Bimetallic Fe-Ni/SiO_2 catalysts for furfural hydrogenation: identification of the interplay between Fe and Ni during deposition-precipitation and thermal treatments

Dichao Shi [a], Qifeng Yang [b], Christi Peterson [c], Anne-Félicie Lamic-Humblot [c], Jean-Sébastien Girardon [a], Anne Griboval-Constant [a], Lorenzo Stievano [d], Moulay T. Sougrati [d], Valérie Briois [e], Paul A. J. Bagot [b], Robert Wojcieszak [a], Sébastien Paul [a], Eric Marceau [a,c,*]

[a] *Univ. Lille, CNRS, Centrale Lille, ENSCL, Univ. Artois, UMR 8181 - UCCS - Unité de Catalyse et Chimie du Solide, F-59000 Lille, France*

[b] *Department of Materials, University of Oxford, Parks Road, Oxford OX1 3PH, United Kingdom*

[c] *Sorbonne Université, CNRS UMR 7197, Laboratoire de Réactivité de Surface, LRS, 4 place Jussieu, F-75252 Paris cedex 05, France*

[d] *Institut Charles Gerhardt Montpellier, CNRS UMR 5253, Université de Montpellier, Pl. E. Bataillon, F-34095 Montpellier cedex 5, France*

[e] *Synchrotron SOLEIL, CNRS-UR1, L'Orme des Merisiers, BP48, Saint-Aubin, F-91192 Gif-sur Yvette, France*

---

*Corresponding author: Dr. Eric Marceau, at the address above,

e-mail: eric.marceau@univ-lille.fr

Abstract

Supported Fe-Ni catalysts have been reported for their activity and selectivity in the hydrogenation of unsaturated organic molecules. However, the control of the size and composition of the bimetallic nanoparticles remains a bottleneck when oxide-supported catalysts are prepared by impregnation, and alternative procedures should be investigated. Starting with Ni(II) and Fe(II) sulfates as precursor salts, deposition-precipitation with urea (DPU) on SiO_2 in an inert atmosphere initially leads to the formation of an ill-crystallized Fe-containing Ni(II) 1:1 phyllosilicate, which reduces under hydrogen at 700°C into bimetallic *fcc* Fe-Ni nanoparticles of 5.4 nm in average. Compared with the composition of the DPU solution (50 Fe at %, 50 Ni at %), an excess of Ni is detected on the catalyst (32 Fe at %, 68 Ni at %), due to the preferential reaction of Ni^{2+} ions with silica. *In situ* X-ray absorption spectroscopy and ^{57}Fe Mössbauer spectroscopy show that the reduction of Fe ions to the metallic state is triggered by the formation of reduced Ni centers above 350°C, and, from then, proceeds progressively, resulting in an excess of Fe in the outer shells of the bimetallic particles. The composition of individual Fe-Ni particles evidences a standard deviation of 8%. The bimetallic Fe-Ni/SiO_2 catalyst gives high yields in furfuryl alcohol in the hydrogenation of furfural, in contrast with an analog Ni/SiO_2 catalyst that favours side-reactions of etherification, hydrogenolysis and hydrogenation of the furan ring.

Keywords

bimetallic catalysts; furfural; X-ray absorption spectroscopy; Mössbauer spectroscopy; in situ measurements

1. Introduction

Noble metals have long been used in catalysis for the hydrogenation of organic molecules, but their natural abundance is low and, consequently, their cost is high and subject to large variations. Substitutes should be found among more abundant and cheaper transition metals. Fe is abundant, but it is also poorly active and poorly stable. In contrast, Ni is known for its activity, but it faces deactivation by carbon, and can favour hydrogenolysis or overhydrogenation side-reactions. However, associating Fe and Ni in supported bimetallic catalysts has been found to be beneficial in terms of activity and selectivity for reactions between H_2 and ketones [1,2], aldehydes [2-5], esters [6,7], phenols [8] or nitriles [1,9]. $Fe_{25}Ni_{75}/SiO_2$ (formulations are herein given in molar proportions) was first mentioned by Khumbar et al. to be more active than Ni/SiO_2 in the hydrogenation of acetophenone and nitriles [1]. More recently, Yu et al. have reported that 5-hydroxymethyl furfural was almost quantitatively hydrogenated into the corresponding diol at 110°C with Fe-Ni catalysts, while the selectivity was lower than 80% with a monometallic Ni catalyst [4].

The structure of reduced Fe-Ni nanoparticles is strongly dependent on the Fe/Ni ratio. Fe-rich nanoparticles exhibit a *bcc* structure while Ni-rich alloys belong to the *fcc* type [10]. Furthermore, as recently reviewed by Tomishige *et al.* [11], the particles sizes are often not uniform when the catalyst is prepared by co-impregnation, and can exceed 10 nm. The control of the Fe/Ni ratio in individual nanoparticles is also difficult. Monometallic nanoparticles, and bimetallic Fe-rich and Ni-rich nanoparticles, may co-exist in the catalyst [1,4,12-15]. If the association between the two metals is not effectively controlled, it can be difficult to link the best catalytic results to precise Fe and Ni proportions in the catalyst formulation.

The thermal treatment of mixed Fe-Ni phases such as hydrotalcites appears to lead to well-defined systems [11,16,17]. In a few instances, deposition-precipitation has been

implemented to yield oxide-supported Fe-Ni nanoparticles of controlled size. The decomposition of co-precipitated Fe and Ni cyanides allowed van de Loosdrecht *et al.* to attain particles sizes smaller than 4 nm on TiO_2 [18]. Deposition-precipitation involving the decomposition of urea (DPU) was recently tested on alumina by Mutz *et al.* [17], resulting in a particle size distribution ranging from 2 to 7 nm for the $Fe_{25}Ni_{75}$ formulation, but the speciation of the metals in the first stages of the DPU process was not described.

DPU has been thoroughly investigated as a method to prepare well-dispersed monometallic Ni nanoparticles on silica, even at metal loadings as high as 40 wt.% [19-22]. Its extension to Fe-based bimetallic nanoparticles raises the question of the association between the two metals upon deposition and thermal treatments. We discuss here the choice of the synthesis parameters required to avoid early metal segregation during DPU, and we evidence the interplay existing between Fe and Ni-containing species along the preparation of a Fe-Ni/SiO_2 catalyst. A combination of *in situ* characterization techniques (X-ray diffraction – XRD; X-ray absorption spectroscopy – XAS; Mössbauer spectroscopy - MössS) is associated to overcome the difficulty to distinguish the two poorly Z-contrasting metals, as conventional transmission electron microscopy or EXAFS alone could not differentiate between two elements with close numbers of electrons. Quick-X-ray absorption spectroscopy recorded simultaneously at the Ni and Fe K edges in *in situ* conditions will provide information on the evolution of the oxidation state and chemical environment of the two metals after DPU and during reduction, while Mössbauer spectroscopy will give valuable data on the speciation of ionic and metallic Fe at all stages of the preparation.

2. Experimental

2.1 Catalysts preparation

A $Fe_{50}Ni_{50}/SiO_2$ catalyst (in which 50/50 represents the relative atomic proportions of the two metals in the initial solution) was prepared using a modified DPU procedure originally developed for Ni/SiO_2 catalysts [19-23]. Sipernat-50 silica (Degussa; surface area, 400 m^2 g^{-1}, pore volume, 1.4 cm^3 g^{-1}) was used as a support. Metal salts used were iron (II) sulfate heptahydrate (Alfa Aesar, 98%), nickel (II) nitrate hexahydrate (Merck, 99%) and nickel (II) sulfate hexahydrate (Aldrich, 99%). Other reactants were nitric acid (Prolabo, 70%), sulphuric acid (Alfa Aesar, 93-98%) and urea (Alfa Aesar, 99-100%). All reactants were used without further purification.

150 mL of aqueous solution of 0.84 mol L^{-1} urea, 0.02 mol L^{-1} H^+ introduced via a strong acid, 0.14 mol L^{-1} Ni(II) salt, 0.14 mol L^{-1} Fe(II) salt, were mixed with 1.14 g of silica in a three-necked flask allowing Ar bubbling. The suspension was continuously stirred and slowly heated to 80°C, resulting in the decomposition of urea, increase of the pH to 5.3, and deposition-precipitation of metallic compounds onto the support. The suspension was kept at 80°C for 22 h. After cooling to room temperature (RT), the solid was recovered by centrifugation, washed three times with distilled water and dried at RT. The choice of the reactants, their order of introduction, and the conditions of washing, drying and storage are discussed in section 3.1. The catalyst was reduced by heating in a flow of 10% H_2/He (100 mL min^{-1}) at 5°C min^{-1} up to 700°C (with a plateau of 2 h), without intermediate calcination.

A Ni_{100}/SiO_2 catalyst was prepared as a reference following the same procedure (Ni(II) concentration in solution: 0.28 mol L^{-1}). It was verified by transmission electron microscopy that, in line with formerly reported results on this system [21,22], the sizes and distribution on the support of metal particles were similar to those of $Fe_{50}Ni_{50}/SiO_2$. Two reference systems providing other Fe/Ni proportions (0.21 mol L^{-1} Fe(II) sulfate, 0.07 mol L^{-1} Ni(II) sulfate;

0.07 mol L^{-1} Fe(II) sulfate, 0.21 mol L^{-1} Ni(II) sulfate), and a reference Co-Ni/SiO_2 system prepared from 0.14 mol L^{-1} Ni(II) nitrate hexahydrate and 0.14 mol L^{-1} Co(II) nitrate hexahydrate (Sigma Aldrich, 98%), were prepared for the sake of comparison, for the characterization of the dried systems (section 3.1) and to support a discussion on metal contents (section 3.2), respectively.

2.2 Characterization

Fe, Ni and Si elemental analysis was performed by inductively coupled plasma-optic emission spectroscopy using a 720-ES ICP-OES spectrometer (Agilent) with axial viewing and simultaneous CCD detection. N_2 physisorption isotherms at liquid nitrogen temperature were carried out on a TriStar II Plus gas adsorption analyzer (Micromeritics) after activation at 150 °C in vacuum overnight. The specific surface area was evaluated with the Brunauer-Emmett-Teller (BET) model over the range P/P_0 = 0.05–0.30. The total pore volume was measured from the volume of N_2 adsorbed at P/P_0 = 0.95. Temperature-programmed reduction (TPR) was followed using an Autochem apparatus (Micromeritics) under H_2 (5%)/Ar (flow rate: 50 mL min^{-1}; ramp rate: 7.5 °C min^{-1}). Attenuated Total Reflection Infra-Red (ATR-IR) spectra were recorded using a Nicolet Magna iS50 spectrometer equipped with a diamond crystal and a DTGS detector (10 scans; resolution: 4 cm^{-1}).

X-ray diffraction patterns (XRD) were recorded in ambient conditions using the Cu Kα radiation (λ = 1.5418 Å; 40 kV, 30 mA) on a Siemens D5000 diffractometer, with a 0.05° scan step and 2 s time step. *In situ* measurements were conducted under H_2 (3%)/N_2 on a D8 Bruker diffractometer equipped with an Anton Paar XRK900 reactive chamber. Data were acquired in the Bragg-Brentano geometry, using the Cu Kα radiation (40kV, 40mA). Diffractograms were recorded every 25 ˚C from 50 to 700 ˚C. A peak from the holder at 2θ = 27.2° was used for calibration between different experiments. The average size of metal

nanoparticles was evaluated by the Laue-Scherrer equation applied to the (111) reflection.

^{57}Fe Mössbauer spectra (MössS) were measured with a source of ^{57}Co embedded in a rhodium metal matrix. Measurements were performed in the transmission mode, with the source at room temperature. The measured sample, in the form of a self-supported pellet, was mounted in an *in situ* oven working at controlled temperatures up to 700°C under diluted H_2 flow. The gas flow was maintained during cooling to 25°C for recording of the spectrum at RT. Low temperature spectra (-268 °C) were measured after transferring the sample pellet to a helium gas flow cryostat in an Ar-filled glove box (O_2, H_2O < 1 ppm), strictly avoiding any contact with ambient air. The spectrometer was operated with a triangular velocity waveform, and a gas-filled proportional counter was used for the detection of the gamma rays. Velocity calibration was performed with an α-Fe foil. The isomer shift δ, the electric quadrupole splitting Δ, the magnetic hyperfine field B_{HF}, the linewidth at half maximum Γ and the relative absorption area of the different components were determined by fitting the spectra with the appropriate combinations of Lorentzian profiles.

Time-resolved XAS data were measured in the transmission mode at the ROCK beamline [24] using the SOLEIL home-made Quick-EXAFS monochromator equipped with a Si (111) channel-cut crystal and described in ref. [25]. The channel-cut oscillates with a ± 1.95° amplitude around 14.6 ° and with a frequency of 2 Hz, allowing simultaneous recording of the Fe (7112 eV) and Ni (8333 eV) K-edge spectra in 250 ms. Successive spectra collected with upward Bragg angles during the *in situ* monitoring of catalysts were merged to improve the signal-to-noise ratio, leading to a time resolution of 5 s per spectrum effectively analyzed. Ionization chambers provided by Ohyo Koken Kogyo Co. Ltd. filled with a 2:1 mixture of N_2 and He were used for measurements. The beam size was 2.5 x 0.5 mm. Normalization of spectra was performed by using the Python normal_gui graphical interface developed at SOLEIL for the fast handling of Quick-XAS data. The proportions of the different Fe and Ni

species were determined by a multivariate data analysis, the MCR-ALS method [26-28]. MCR-ALS GUI 2.0 developed by the Tauler group [29], and freely available as a Matlab toolbox, was used for MCR-ALS minimization. The EXAFS signal extraction and Fourier transformation of the EXAFS spectra were done using the Athena graphical interface software [30]. EXAFS fitting of distances, coordination numbers and Debye–Waller factors was performed with the Artemis interface to IFeFFIT using least-squares refinements [31], firstly checked on NiO, Ni metallic foil and Fe_2O_3 references. Fourier-transformed EXAFS signals are presented without phase correction. The temperature-programmed reduction of the $Fe_{50}Ni_{50}/SiO_2$ sample was performed using a dedicated cell [32] connected to the gas-feeding system installed on the ROCK beamline. The cavity of the sample holder (2 mm thick) was filled with the powder catalyst (20 mg) pre-mixed with boron nitride (BN, 10 mg). The *in situ* catalyst reduction was performed by heating the cell from RT to 500 °C under a H_2 (5%)/He flow (50 mL min^{-1}) with a heating rate of 5°C min^{-1}, followed by 2 h of isothermal treatment.

TEM observations were made at University of Oxford, using a JEOL JEM-2100 microscope fitted with a LaB_6 source (JEM-2100) for bright field observation, and on a JEM-3000F FEGTEM microscope (JEM-3000) fitted with a spherical aberration STEM probe corrector and a Centurion EDX detector equipped with a super atmospheric thin window (SATW) detector and an INCA processor, for elemental analysis. E-beam size was selected to 1.2 nm for EDX point scan measurements on individual particles.

2.3 Catalytic tests

$Fe_{50}Ni_{50}/SiO_2$ and Ni_{100}/SiO_2 catalysts were tested in the hydrogenation of furfural using a Screening Pressure Reactor (SPR) system from Freeslate equipped with 24 parallel stainless steel batch reactors of 6 mL each. 10 mg of catalysts, reduced at 700°C (section 2.1), were placed after transfer in ambient air into each of the 24 reactors and exposed *in situ* to

pure H_2 at 400°C (1 bar, 2 h) prior to reaction. 2 mL solutions of furfural (0.20, 0.56 or 1.00 mmol) in isopropanol were then injected under the controlled atmosphere of a glove box. Tests were performed at 150°C for 2 h under 20 bar H_2 and a continuous stirring of 700 rpm. Reaction products were analyzed using Shimadzu GC-2010 Plus and GC-FID-MS-QP2010 Ultra EI gas chromatographs, equipped with a FID detector, a ZB-5MS column (30 m × 0.25 mm × 0.25 μm), and for the latter, with a QP2010 Ultra mass spectrometer. It was verified by quantifying acetone that in these experimental conditions, hydrogen transfer from isopropanol to furfural did not occur to a significant extent (less than 3% of converted furfural).

3. Results and discussion

3.1 Choice of the experimental parameters for the synthetic procedure and characterization of dried catalysts

Given the solubility products of iron and nickel hydroxides (pKs $Fe(OH)_3$ = 38.8; $Fe(OH)_2$ = 15.1; $Ni(OH)_2$ = 15.2 at 25°C), Fe^{2+} ions are expected to deposit in the same pH range as Ni^{2+} ions, and Fe^{3+} ions at much lower pH. Fe(II) sulfate was thus selected as the iron precursor salt for DPU, in preference to Fe(III) nitrate. In spite of this, initial attempts of DPU with nickel nitrate as precursor salt and nitric acid as acidifier led to the oxidation of Fe(II) to Fe(III) upon heating, as evidenced by the change of colour of the suspension from green to orange, and to the early, separate precipitation of well-crystallized goethite $Fe^{III}O(OH)$ at pH 4.8, from which large particles of metallic *bcc* Fe would later grow upon reduction (diffraction peaks at 2θ = 44.8 and 65.0°, (110) and (200) reflections; size: 40 nm). In order to eliminate oxidizing species, nickel (II) sulfate and sulphuric acid were instead used as reactants, but the preparation still suffered from a lack of reproducibility. Diffraction peaks of Fe(III)-containing layered hydroxysulfate phases [33-35] were observed after drying, with ulterior formation of large Fe-Ni particles upon reduction (**Fig. S1**, Supplementary Material).

It was next chosen to degas with Ar the suspension containing silica, sulphuric acid, nickel (II) sulfate and urea for 2 h, and to introduce Fe (II) sulfate only after degassing. Ar bubbling was maintained during the whole heating and cooling steps. In these conditions, deposition took place at pH 5.3 and the suspension remained green. Centrifugation and washing were also carried out with degassed water.

Drying at RT in ambient air caused a rapid change of colour of the solid from green to ochre, evidencing the oxidation of Fe(II) to Fe(III). Such oxidation is prone to happen to Fe(II)-containing layered hydroxides [36-38]; it has been shown that the presence of Ni(II) ions inhibits their further transformation to Fe_3O_4 [39,40]. Drying the solid under Ar flow in the three-necked flask, and storage under Ar, preserved the green colour longer, but oxidation of iron to Fe(III) was nevertheless seen to develop over a period of six weeks. Using XRD and XAS, it was checked by reducing dried solids either kept under Ar or aged in air that, unlike Fe oxidation during DPU, Fe oxidation upon drying and storage had no detrimental effect on the formation, nature and size of the reduced metal nanoparticles.

The XRD pattern of all dried solids exhibits a broad diffraction peak at about 22°, characteristic of amorphous siliceous solids, a broad asymmetrical line at $2\theta = 34^\circ$ and a narrow symmetrical one at $2\theta = 60^\circ$ (**Fig. S1)**. As previously shown for Ni/SiO_2 catalysts prepared by DPU, the latter two peaks can be assigned to structures based on brucitic layers, either $M^{II}(OH)_2$ turbostratic hydroxides or ill-crystallized phyllosilicates [19].

MössS confirms the exclusive presence of octahedral Fe(III) ions in dried $Fe_{50}Ni_{50}/SiO_2$ after exposure to air (**Fig. 1a**, **Table 1**). The signal recorded at RT is asymmetric and must be fitted with at least two different quadrupole split contributions, as is often done for ions present in a continuum of environments. Given the relatively narrow range of isomer shifts and quadrupole splittings for octahedral Fe(III), it is virtually impossible to distinguish between Fe(III) oxyhydroxides and silicates [41]. However, the absence of a

sextet allows discarding the presence of well-crystallized goethite FeOOH, which is expected to exhibit magnetic order at room temperature [42,43]. Moreover, the relatively low isomer shift of the narrow doublet, close to that measured for octahedrally coordinated iron in mixed metal Ni-Fe ferrites, suggests the formation of mixed-metal species [44]. To test this hypothesis, Mössbauer spectra were recorded on dried solids prepared following the same protocol but with two other Fe and Ni nominal contents (**Fig. S2**, **Table S1**). The significant changes in the quadrupole splittings, as well as the slight decrease of the average isomer shift when changing the metal contents, suggests that Fe(III) ions are co-deposited with Ni(II) ions. Finally, electric quadrupole splittings are noticeably larger here than in well-defined oxyhydroxides and silicates, especially that of the second doublet. This is usually interpreted as the sign of distorsions in the chemical environment: distorted octahedra, surface sites, proximity to tetrahedral sites or to divalent cations, such as Ni^{2+}, in hydroxides or silicates [39,42,45-47].

According to the analysis of EXAFS oscillations, the local environment of both Fe^{3+} and Ni^{2+} ions is consistent with the octahedral sites of brucitic layers, common to the structures of divalent hydroxides and phyllosilicates [19] **(Fig. 2, Fig. S3, Table 2**). The first shell is satisfactorily fitted using 6 oxygen atoms (R = 1.99 Å for Fe^{3+}, R = 2.05 Å for Ni^{2+}), probably in a more distorted symmetry in the case of Fe(III) as shown by the higher value of the Debye-Waller factor. The best fits for the second shell of neighbours involve 6 Ni atoms at R = 3.11 Å, characteristic of edge-sharing octahedra (it must be noted though that, due to the closeness of scattering phase and amplitude functions for Fe and Ni, the nature of the second neighbours as backscatterers cannot be unambiguously discriminated by EXAFS). If existing, iron environments involving two very different Fe-Fe distances above 3 Å, as encountered in FeOOH phases [46,48,49], are not predominant.

3.2 Evolution and composition of the phases deposited during DPU

The nature of the deposited phases and the metal contents were investigated as a function of DPU duration, from 1 to 22 h. While the X-ray diffractograms did not exhibit major changes besides the gradual broadening of the large halo associated to silica (**Fig. S4**), the evolution of ATR-IR bands (**Fig. 3a**) revealed that, following the pattern reported for monometallic Ni/SiO_2 catalysts [19], the brucitic $M^{II}(OH)_2$ phase formed during the first 4 h of DPU evolved into an ill-crystallized 1:1 phyllosilicate. This is proved by (1) the progressive growth of the asymmetrical doublet of bands at 1007 and 1083 cm^{-1} (υ(Si-O) stretching vibration in a 1:1 phyllosilicate); (2) the decrease of the weak asymmetrical υ(Si-OH) band originating from silica at 974 cm^{-1}; (3) the shift and decrease of the intensity of the υ(Si-O) vibration band assigned to silica at *ca.* 800 cm^{-1}; (4) the decrease of the δ(OH) band at 640 cm^{-1}, characteristic of turbostratic $M^{II}(OH)_2$, between 2 and 4 h, and, (5) from 4 h, the increase of a broad band at 664 cm^{-1} assigned to a tetrahedral Si-O mode in the 1:1 phyllosilicate structure. The poor crystallinity of the phyllosilicate phase may explain the absence of detection of Si second-shell neighbours in the EXAFS fits.

ICP measurements indicate that, despite the equimolarity between Fe and Ni in solution, nickel is the main metal initially depositing during the first hours (**Fig. 3b**). After a moderate drop between 1 and 4 h, the nickel content increases by a two-fold between 4 and 8 h, when the phyllosilicate phase forms. In contrast, the Fe content steadily increases throughout the process. As a result, a significant excess of nickel with respect to iron is present after 22 h DPU in the dried solid, compared with the atomic proportions in solution: 38 Fe at % and 62 Ni at % are measured by ICP on the solid, corresponding to 42% of the amount of Fe and to 67% of the amount of Ni initially introduced in solution.

This excess of nickel does not originate from its early introduction in the DPU solution, as it was also observed when nickel and iron sulfates were added together in solution after Ar degassing. For the sake of comparison, a reference system was prepared from nickel and cobalt (II) nitrates (nominal proportions: 50 Co at % and 50 Ni at %), without degassing and separate introduction of the reactants. The atomic proportions given by EDX measurements (34 Co at %, 66 Ni at %) prove that nickel tends to react with silica preferentially, compared with the other metal.

Finally, no IR band assigned to isocyanates or carbonates was observed in the spectra. A shoulder at 607 cm^{-1} could be assigned to sulfate ions (ν_4 vibration mode [50,51]), but it was verified by ICP and XPS that sulfate ions were not detected on the dried solid.

In summary, the early precipitation of $Ni(OH)_2$ onto silica during the first hours of DPU is followed by the formation of a poorly organized 1:1 phyllosilicate, in which, after drying, Fe^{3+} and Ni^{2+} ions occupy the octahedral layer. The (Fe+Ni)/Si ratio of 1.3 after 22 h of DPU is consistent with a 1:1 phyllosilicate stoichiometry (M/Si ratio varying between 1 and 1.5 for exclusively trivalent and divalent cations, respectively). In the absence of carbonates or sulfates, charge compensation can be ensured by deprotonation of the layers, and formation of O^{2-} or OH^- anions formed upon oxidation of iron during drying and storage. FeOOH as a separate phase is not predominant, but the existence of minor domains cannot be excluded as MössS evidences a distribution of environments around Fe^{3+} ions.

3.3 Reduction process

The temperature-reduction profile of $Fe_{50}Ni_{50}/SiO_2$ (after storage in ambient air and drying at 60°C to eliminate adsorbed water) evidenced three main reduction stages (**Fig. S5**): a minor one between 270 and 350°C, and two major ones between 350 and 500°C, and

between 500 and 700°C, respectively. *In situ* X-ray absorption spectroscopy and Mössbauer spectroscopy were used to link these events to the reduction of Fe and Ni-containing species. On the basis of the TPR profile, 700°C was selected as the reduction temperature at which both metals were expected to be quantitatively reduced.

The reduction of air-stored $Fe_{50}Ni_{50}/SiO_2$ was monitored simultaneously at the Ni and Fe K edges by *in situ* XAS up to 500°C, the upper temperature limit allowed by the set-up (**Fig. 4a** and **b**). In line with the presence of a set of isosbestic points on the series of spectra recorded at the Ni K edge, the quantitative analysis by MCR-ALS procedure (whose principle is recalled in the Supplementary Material) requires two spectral components only (**Fig. 4c**, **Fig. S6**), that recall the experimental spectrum of Ni^{2+} ions in the initial phyllosilicate, and that of metallic *fcc* Ni as confirmed by the EXAFS analysis of the final state (**Fig. 2b** and **c**, **Fig. S3b** and **c**, **Table 2**). The reduction of Ni^{2+} ions starts above 350°C, with an inflection point at 400°C. Nickel reduction is complete after a plateau of 1 h at 500°C. The absence of an intermediate dehydrated phase in the analysis is justified by the higher temperature range at which nickel phyllosilicate would decompose to NiO (500-600°C) [22].

The progress of iron reduction, deduced from the spectra recorded at the Fe K edge, is more complex to analyse. The lack of isosbestic points indicates that more than 2 components are involved in the reduction, and the EXAFS signal of the final state could not be satisfactorily fitted with a limited set of parameters. It was thus chosen in a first approach to follow the decrease in energy of the Fe edge position, correlated to a decrease of the Fe oxidation state (**Fig. 4d**). The position in energy of the edge was interpreted with respect to reference compounds: hematite Fe_2O_3, Fe(II) sulfate, Fe foil. Fe^{3+} ions originally present inside the layered structure underwent an accelerated reduction to Fe^{2+} in the 275-350 °C temperature range. A more gradual decrease of the edge value above 350°C, starting when Ni reduces to the metallic state, can be interpreted as a progressive reduction of Fe^{2+} iron to Fe

metal triggered by Ni reduction. A comparison between the final XANES spectrum and the spectrum of reference metallic Fe shows that the reduction of Fe^{2+} is not complete at the end of the plateau at 500°C.

The MCR-ALS analysis of Fe reduction provides five independent spectral components (**Supp. Mater.**, **Fig. S7** and **S8**). The white lines of the first two components are identical, and the EXAFS oscillations are found at the same energies, though damped for the second component. The third component appears between 275 and 358°C. As seen above, the lower edge energy is associated to the Fe(II) oxidation state. The EXAFS oscillations are similar to those of the first component, though shifted to lower energies. The Fourier transforms of the first three components resemble each other, apart from the decrease of intensity of the peaks due to a temperature-induced increase of the Debye-Waller parameter. The Fourier transform of the third component also differs from those recorded on oxides such as Fe_3O_4. This suggests that the set of the first three components is related to the same phase, i.e., the Fe-containing phyllosilicate, the second component reflecting mostly an increase of disorder with temperature (data related to the first two components are provided in **Fig. S9** and **Table S2**), and the third component a reduced Fe^{2+} state of iron ions in the layered phase. The first event observed on the TPR profile is thus linked to the reduction of Fe^{3+} to Fe^{2+}.

The third component starts disappearing when nickel reduction starts, while the fourth component appears exactly in parallel with the formation of metallic nickel. The position in energy of the edge of the fourth component lets one assume that it is associated to Fe^{2+} ions, though in a strongly altered environment: the shape of the first peak in the Fourier transform, which seems to contain both Fe-O and Fe-Fe (or Fe-Ni) contributions, suggests both the existence of an oxidic phase, and a proximity to metal particles. The last component, whose weight increases gradually during the plateau at 500°C, gives a well-defined Fourier transform identical to that of metallic Ni, and is interpreted as Fe(0) atoms located in the *fcc*

environment of Ni-containing nanoparticles. In view of this last result, the fourth component may be understood as a Fe(II)-containing phase external to the Fe-Ni particles, from which Fe reduces and diffuses into the bimetallic nanoparticles upon increasing temperature and time. These processes and the concomitant reduction of Ni^{2+} to Ni(0) explain the second reduction stage on the TPR profile.

The evolution of the X-ray diffractograms of $Fe_{50}Ni_{50}/SiO_2$ during reduction under H_2 is presented as a function of temperature on **Figure 5**. Only the diffraction peaks of the phyllosilicate phase are visible up to 350°C. In accordance with XAS, three diffraction peaks characteristic of *fcc* metal nanoparticles ((111), (200) and (220) reflections) are detected above 350°C and their intensity increases when temperature increases up to 700°C. No peak related to *bcc* phases is observed (in particular the (200) reflection expected around 2θ = 65.0°). The average size of the crystalline domains increases from 3 to 5 nm from 350 to 700°C. The diffraction peaks attributed to the phyllosilicate phase disappear above 500°C.

The unit cell parameter *a* is known to decrease linearly with increasing Ni content in bimetallic *fcc* Fe-Ni alloys [52], as the atomic radius of Fe (0.172 nm) is larger than that of Ni (0.162 nm). A linear Vegard correlation between *a*, measured at RT, and the Ni atomic content was drawn from the JCPDS files of reference Fe-Ni alloys (**Fig. S10**); an uncertainty of 1 x 10^{-4} nm on the value of *a* leads to an uncertainty of 1 Ni at % in the composition of the diffraction domains. After correction from the temperature-induced shifts measured for monometallic Ni_{100}/SiO_2 in the same conditions (**Fig. S11** and **S12**), the positions of the (111) and (200) reflections for $Fe_{50}Ni_{50}/SiO_2$ give access to the values of *a* at RT after reduction at 500 and 700°C (0.3547 and 0.3557 nm, respectively) and, through the correlation established above, to an assessment of the composition of the crystalline core of the particles ($Fe_{22}Ni_{78}$ and $Fe_{31}Ni_{69}$, respectively). The latter value of *a* is confirmed after measurement back at RT under H_2 (0.3555 nm, $Fe_{29}Ni_{71}$).

The ^{57}Fe Mössbauer spectrum of the sample reduced at 500°C (**Fig. 1b**, **Table 1**) can be interpreted in terms of three components. The isomer shift of the first two large quadrupole split components is typical of high-spin Fe(II) ions, in line with XAS results. The component with the larger quadrupole splitting is consistent with Fe(II) ions in silicates, since the hyperfine parameters correspond to their typical range [53]. The quadrupole splitting of the second component, however, is too small to correspond to a bulk silicate, and can be attributed to Fe(II) ions in extremely distorted octahedral sites, or to lower coordination numbers. The third contribution, covering 57% of Fe, consists of a singlet typical of Fe(0), with an isomer shift at δ = 0.06 mm.s^{-1} slightly more positive than that of iron metal, as reported for Fe-Ni alloys (δ = 0-0.06 mm.s^{-1} at 25°C, the value of δ increasing with the Ni content [54-56]). Based on the overall composition determined by ICP (38 Fe at %, 62 Ni at %), the composition of the Fe-Ni particles at 500°C is evaluated as $Fe_{22}Ni_{78}$, in good agreement with that determined by *in situ* XRD. The absence of a sextet shows that the Fe-Ni nanoparticles are superparamagnetic at RT, thus exhibiting a size smaller than 10 nm [55,56].

The third reduction stage on the TPR profile can be explained by comparing the Mössbauer spectra recorded at 500 and 700°C. Reduction at 700°C (**Fig. 1c and d**, **Table 1**) produces a complete modification of the ^{57}Fe Mössbauer spectrum, which can now be fitted with only two spectral components, a singlet and a quadrupole doublet. Both components are often observed for reduced, superparamagnetic iron nanoparticles, and are usually attributed to bulk and surface iron atoms, respectively [57]. The singlet at δ = 0.04 mm.s^{-1} corresponds to Fe(0) at the core of Fe-Ni nanoparticles. The decrease of δ suggests an environment richer in Fe compared with the reduced state at 500°C [54]. Since the hyperfine parameters of the quadrupole doublet can be confused with those of Fe(III), the same sample was measured at -268°C after transfer in a helium-flow cryostat. The low-temperature spectrum is dominated by a magnetically split contribution, that can be fitted with at least two magnetic sextets,

comprising 90% of total Fe. The isomer shift, once taken into account the second-order Doppler shift, and the magnetic field of these sextets are in the typical range of Fe(0) in Fe-Ni alloys [58]. The two hyperfine fields are close to those measured for *fcc* Fe-Ni alloys in which Ni or Fe is the major metal (29 and 33 T, respectively [59]). In addition to these two components, a minor quadrupole split component accounting for about 10% of the total resonance area is still present at the centre of the spectrum. At this stage, it can be interpreted as Fe(0) species not ordered magnetically, either located at the periphery of bimetallic particles, or in highly dispersed monometallic Fe nanoparticles.

3.4 Characterization of the metal nanoparticles by TEM and EDX after reduction at 500 and 700°C

After reduction at 700°C, the $Fe_{50}Ni_{50}/SiO_2$ catalyst exhibited a specific surface area of 240 $m^2\ g_{catalyst}^{-1}$, an apparently low value compared with pristine silica, but explained mainly by the high metal loading ((Fe+Ni) loading = 52 wt%) and by the deep transformation of silica during DPU. The pore volume was 0.6 $cm^3.g^{-1}$.

The metal nanoparticles on $Fe_{50}Ni_{50}/SiO_2$ were characterized by bright field TEM after reduction at 500 or 700°C, and exposure of the samples to ambient air (**Fig. 6a** and **b**). After reduction at 500°C, they appeared as evenly distributed over the siliceous matrix and exhibited an average diameter of 5.1 nm (standard deviation: 0.9 nm), with a high proportion of smaller particles (**Fig. S13a**). Agglomeration was not observed after reduction at 700°C, and the bimetallic nanoparticles were still evenly distributed on the silica substrate despite the high metal loading, with a separation distance of 5 nm on average. The size distribution histogram shows that the average size, 5.4 nm, has only slightly increased between 500 and

700°C (**Fig. S13b**). The standard deviation was 1.3 nm and the size distribution was more symmetrical, with a lower proportion of smaller particles.

The elemental distribution of Fe and Ni was examined by EDX mapping after reduction at 500°C (**Fig. 6c**). No metal was detected on bare zones of the support. The composition of 28 individual particles was measured, resulting in an average composition of $Fe_{31}Ni_{69}$, and a standard deviation of 8 at % (**Tab. S3**). Both elements were present in every particle and Fe was never the major metal. It was not possible to perform point scans along the diameter of particles, owing to their small size, or to evidence local metal segregation. Moreover, the comparison with *in situ* measurements is not straightforward, as the distribution of the metals may be perturbed by metal oxidation upon exposure to air [17].

DPU applied to the Fe-Ni system thus yields bimetallic nanoparticles of controlled size, in the same range as for monometallic Ni/SiO_2 catalysts [21], and resistant to sintering at high temperature. The reduction above 350°C of the nickel ions from the phyllosilicate phase drives the progressive destruction of the layered structure and the reduction of surrounding iron ions to the metallic state, to form Ni-rich Fe-containing *fcc* nanoparticles. At 500°C, about 40% Fe^{2+} ions are still present in an oxidic environment, in close association with the metal nanoparticles. Their gradual reduction between 500 and 700°C results in the diffusion of more Fe atoms inside the Fe-Ni particles. The composition of the particles, consistent with the values presented in sections 3.1 and 3.2, pertains to a limited range, with a standard deviation of 8 at %. In the absence of monometallic and Fe-rich particles, both the detection of non-magnetically ordered Fe by MössS, and the different values of the magnetic hyperfine field, suggest that a gradient of Fe concentration exists in the bimetallic particles, as formerly postulated by Nagorny and Bubert [59]. Due to the late reduction of Fe, the outer shells surrounding the bimetallic Fe-Ni crystalline core would be enriched in Fe, in line with former

interpretations from the literature based on spectroscopic data and on beta emission from radioactive Ni [14,59-61].

3.5 Catalytic tests

Depending on the catalyst nature and reaction conditions, the hydrogenation of furfural yields a slate of products resulting from the hydrogenation of the aldehyde function (furfuryl alcohol, FFA), hydrogenation of the furan ring (tetrahydrofurfuryl alcohol, THFFA) and/or hydrogenolysis of the C-O bond (2-methylfuran, MF; 2-methyltetrahydrofuran, MTHF) (**Scheme 1**). In the present work, ethers resulting from reactions with the isopropanol solvent were also identified by GC/MS (2-(isopropoxymethyl)furan, iPrOMF, m/z 81, 97, 139; 2-(isopropoxymethyl)tetrahydrofuran, iPrOMTHF, m/z 71, 85, 101, 144). Etherification can proceed with FFA or THFFA as a reaction intermediate, or *via* the direct reductive reaction of furfural, and can be catalyzed by unreduced metal ions acting as Lewis acidic centers [62,63].

$Fe_{50}Ni_{50}/SiO_2$ and Ni_{100}/SiO_2 catalysts were pre-reduced at 700°C, and underwent a second stage of reduction at 400°C prior to reaction to counter the effect of transfer in air. A characteristic TEM bright field micrograph of Ni_{100}/SiO_2, and the size histogram associated to this catalyst, are presented on **Fig. S14**. The metal dispersion D (%) can be calculated for the two catalysts by applying 97.1/Ø (nm) [64] to each class of diameter Ø from the two histograms **(Fig. 6b and S14)**, assuming that metal particles are hemispherical and that this calculation, usually applied to *fcc* Ni, can be extended to *fcc* Fe-Ni alloys. A value of D = 20% is obtained both for $Fe_{50}Ni_{50}/SiO_2$ and Ni_{100}/SiO_2. The metal surface area exposed per gram of catalyst is evaluated as 70 $m^2\ g_{cat}^{-1}$, assuming that one Fe or Ni atom occupies 6.3 $Å^2$ [64].

In the given experimental conditions, both catalysts showed high activity in the hydrogenation of furfural at 150°C (conversion: 97-100%), whatever the starting amount of furfural in solution (**Table 3**). In contrast, yields were highly impacted by several factors. Monometallic Ni_{100}/SiO_2 was rather selective to THFFA and MTHF, the over-hydrogenated products, in good correlation with the literature in similar conditions of temperature and pressure [5,65,66]. The formation of MF and MTHF by hydrogenolysis was favoured when the initial amount of furfural was high. Etherification of the alcohols appeared prominent. As a result, the yield of FFA from the hydrogenation of the carbonyl group remained very low, which can be explained by its conversion to MF by hydrogenolysis.

Unlike monometallic Ni_{100}/SiO_2, the $Fe_{50}Ni_{50}/SiO_2$ catalyst exhibited a high yield in FFA whatever the initial amount of furfural, and low yields of THFFA, MF and MTHF. The carbon balance was high, demonstrating that lower amounts of heavy products were formed than with the monometallic Ni system. The fraction of ether formed from FFA slightly increased with the amount of furfural, but remained minor except when the catalyst did not undergo a pre-reduction at 700°C and thus contained iron mainly in an ionic form. As has been reported in the literature, the hydrogenation of the carbonyl group reaction prevails on the hydrogenation of ring and hydrogenolysis reactions on Fe-Ni catalysts [4,5]. The role of Fe surface atoms in the suppression of Ni overhydrogenating and hydrogenolyzing properties is thus confirmed here.

4. Conclusions

The preparation of bimetallic Fe-Ni/SiO_2 catalysts by deposition-precipitation with urea requires the use of a Fe(II) salt and the absence of oxidizing species such as nitrates or dissolved oxygen. A layered structure best described as an ill-crystallized Fe-containing Ni(II)

1:1 phyllosilicate is formed after 22 h of DPU, with a lower proportion of Fe compared with the composition of the DPU solution (32 Fe at %, 68 Ni at %, against 50 Fe at %, 50 Ni at %), due to a preferential reaction of Ni^{2+} ions with silica. The oxidation of Fe^{2+} to Fe^{3+} upon drying and storage does not challenge the subsequent formation of bimetallic particles upon reduction. Reduction under H_2 proceeds in several stages: (1) reduction of Fe^{3+} ions to Fe^{2+} above 275°C; (2) reduction of Ni^{2+} to Ni(0) above 350°C, triggering the progressive reduction of Fe^{2+} ions to the metallic state, and the insertion of a fraction of Fe atoms into the *fcc* structure of Ni-rich particles; (3) deeper reduction of Fe^{2+} ions between 500 and 700°C, resulting both in the diffusion of Fe atoms in the Fe-Ni core of the *fcc* particles, and in the enrichment in Fe of their outer shells. After reduction at 700°C, the bimetallic particles are homogeneous in size (average size: 5.4 nm) despite the elevated reduction temperature, and exhibit a standard deviation of composition of 8 Fe at %. The enrichment in Fe of the surface of the Fe-Ni nanoparticles suppresses hydrogenolysis and overhydrogenation side-reactions observed for Ni/SiO_2 in the hydrogenation of furfural, and provides a catalyst selective in furfuryl alcohol. Side-reactions of etherification with the isopropanol solvent may be linked to the presence of unreduced metal ions acting as Lewis acidic sites.

Acknowledgements

This work has benefited from the support of the CSC-Ecole Centrale de Lille PhD scholarship program (D. S.), of the REU exchange program from the National Science Foundation (C. P.), and of the French National Research Agency (ANR), through the NobleFreeCat project (ANR-17-CE07-0022). Chevreul Institute (FR 2638), Ministère de l'Enseignement Supérieur et de la Recherche, Région Hauts-de-France and FEDER are acknowledged for supporting and funding partially this work.

Joelle Thuriot-Roukos (ICP), Jean-Charles Morin (ATR-IR), Olivier Gardoll (TPR), Svetlana Heyte (SPR/GC-MS), Pascal Roussel and Laurence Burylo (*in situ* XRD) at UCCS, as well as Alban Charlier (preparation of the reference Co-Ni catalyst) at LRS, are thanked for their help.

XAS experiments were performed on the ROCK beamline, using the Chemistry support lab, at SOLEIL Synchrotron, France (proposal number 20151218). The ROCK beamline is benefiting from a public grant overseen by the French National Research Agency (ANR) as a part of the 'Investissements d'Avenir' program (PIA) with the contractual reference 'ANR-10-EQPX-45'. Camille La Fontaine is thanked for his help on the beamline. The authors acknowledge the European microscopy network ESTEEM 2 for funding access to the microscope platform in Oxford (project 20150908), and Dr. Neil P. Young (University of Oxford) for his help.

The REALCAT platform is benefitting from a state subsidy administrated by the French National Research Agency (ANR) within the frame of the 'Future Investments' program (PIA), with the contractual reference 'ANR-11-EQPX-0037'. The European Union, through the ERDF funding administered by the Hauts-de-France Region, has co-financed the platform. Centrale Lille, the CNRS, and University of Lille as well as the Centrale Initiatives Foundation, are thanked for their financial contributions to the acquisition and implementation of the equipment.

The authors declare no competing interests.

References

[1] P. Khumbar, M.R. Kharkar, G.D. Yadav, R.A. Rajadhyaksha, J. Chem. Soc., Chem. Commun. (1992) 584-586.

[2] G. Chieffi, C. Giordano, M. Antonietti, D. Esposito, J. Mater. Chem. A 2 (2014) 11591-11596.

[3] S. Sitthisa, W. An, D.E. Resasco, J. Catal. 284 (2011) 90-101.

[4] L. Yu, L. He, J. Chen, J. Zheng, L. Ye, H. Lin, Y. Yuan, ChemCatChem 7 (2015) 1701-1707.

[5] W.S. Putro, T. Kojima, T. Hara, N. Ichikuni, S. Shimazu, Catal. Sci. Technol. 7 (2017) 3637-3646.

[6] S. Leng, X. Wang, X. He, L. Liu, Y. Liu, X. Zhong, G. Zhuang, J. Wang, Catal. Commun. 41 (2013) 34-37.

[7] X. Yu, J. Chen, T. Ren, RSC Adv. 4 (2014) 46427-46436.

[8] H. Fang, J. Zheng, X. Luo, J. Du, A. Roldan, S. Leoni, Y. Yuan, Appl. Catal. A 529 (2017) 20-31.

[9] G.D. Yadav, M.R. Kharkara, Appl. Catal. A 126 (1995) 115-123.

[10] L J. Swartzendruber, V.P. Itkin, C.B. Alcock, J. Phase Equilibr. 12 (1991) 288-312.

[11] K. Tomishige, D. Li, M. Tamura, Y. Nakagawa, Catal. Sci. Technol. 7 (2017) 3952-3979.

[12] E.E. Unmuth, L.H. Schwartz, J.B. Butt, J. Catal. 61 (1980) 242-255.

[13] C.N.R. Rao, G.U. Kulkarni, K.R. Kannan, S. Chaturvedi, J. Phys. Chem. 96 (1992) 7379-7385.

[14] L. Wang, D. Li, M. Koike, S. Koso, Y. Nakagawa, Y. Xu, K. Tomishige, Appl. Catal. A 392 (2011) 248-255.

[15] J. Ashok, S. Kawi, Appl. Catal. A 490 (2015) 24-35.

[16] S.M. Kim, P. Macarena Abdala, T. Margossian, D. Hosseini, L. Foppa, A. Armutlulu, W. van Beek, A. Comas-Vives, C. Copéret, C. Müller, J. Am. Chem. Soc. 139 (2017) 1937-1949.

[17] B. Mutz, M. Belimov, W. Wang, P. Sprenger, M.A. Serrer, D. Wang, P. Pfeifer, W. Kleist, J.D. Grunwaldt, ACS Catal. 7 (2017) 6802-6814.

[18] J. van de Loosdrecht, A.M. van der Kraan, A.J. van Dillen, J.W. Geus, Catal. Lett. 41 (1996) 27-34.

[19] P. Burattin, M. Che, C. Louis, J. Phys. Chem. B 101 (1997) 7060-7074.

[20] P. Burattin, M. Che, C. Louis, J. Phys. Chem. B 102 (1998) 2722-2732.

[21] P. Burattin, M. Che, C. Louis, J. Phys. Chem. B 103 (1999) 6171-6178.

[22] P. Burattin, M. Che, C. Louis, J. Phys. Chem. B 104 (2000) 10482-10489.

[23] L.A.M. Hermans, J.W. Geus, in Preparation of Catalysts II (B. Delmon, P. Grange, P.A. Jacobs, G. Poncelet, Eds.), Elsevier, Amsterdam, 1979, p. 113.

[24] V. Briois, C. La Fontaine, S. Belin, L. Barthe, T. Moreno, V. Pinty, A. Carcy, R. Girardot, E. Fonda, J. Phys.: Conf. Ser. 712 (2016) 012149.

[25] E. Fonda, A. Rochet, M. Ribbens, L. Barthe, S. Belin, V. Briois, J. Synchrotron Radiat. 19 (2012) 417–424.

[26] W.H. Cassinelli, L. Martins, A.R. Passos, S.H. Pulcinelli, C.V. Santilli, A. Rochet, V. Briois, Catal. Today 229 (2014) 114–122.

[27] J. Hong, E. Marceau, A.Y. Khodakov, L. Gaberová, A. Griboval-Constant, J.S. Girardon, C. La Fontaine, V. Briois, ACS Catal. 5 (2015) 1273-1282.

[28] A. Rochet, B. Baubet, V. Moizan, C. Pichon, V. Briois, C. R. Chim. 19 (2016) 1337–1351.

[29] J. Jaumot, A. de Juan, R. Tauler, Chemom. Intel. Lab. Syst. 140 (2015) 1-12.

[30] B. Ravel, M. Newville, J. Synchrotron Radiat. 12 (2005) 537–541.

[31] M. Newville, J. Synchrotron Radiat. 8 (2001) 322–324.

[32] C. La Fontaine, L. Barthe, A. Rochet, V. Briois, Catal. Today 205 (2013) 148–158.

[33] J.D. Bernal, D.R. Dasgupta, A.L. Mackay, Clay Miner. Bull. 4 (1959) 15-30.

[34] E.H. Nickel, J.E. Wildman, Mineral. Mag. 44 (1981) 333-337.

[35] L.H. Garófalo Chaves, J.E. Curry, D.A. Stone, M.D. Carducci, J. Chorover, Rev. Bras. Ci. Solo 33 (2009) 1115-1123.

[36] J.M.R. Génin, R. Aïssa, A. Géhin, M. Abdelmoula, O. Benali, V. Ernstsen, G. Ona-Nguema, C. Upadhyay, C. Ruby, Solid State Sci. 7 (2005) 545-572.

[37] J.M.R. Génin, A. Renard, C. Ruby, M. Abdelmoula, J. Phys.: Conf. Ser. 217 (2010) 012095.

[38] X. Wang, F. Liu, W. Tan, X. Feng, L. K. Koopal, Chem. Geol. 351 (2013) 57-65.

[39] P. Refait, H. Drissi, Y. Marie, J.M.R. Génin, Hyperfine Interact. 90 (1994) 389-394.

[40] K.W. Chung, Y.T. Kho, K.B. Kim, Corros. Sci. 44 (2002) 2757-2775.

[41] F. Menil, J. Phys. Chem. Solids 46 (1985) 763-789.

[42] M.L.M. de Carvalho-e-Silva, C.S.M. Partiti, J. Enzweiler, S. Petit, S.M. Netto, S.M.B. de Oliveira, Hyperfine Interact. 142 (2002) 559-576.

[43] M. Usman, M. Abdelmoula, K. Hanna, B. Grégoire, P. Faure, C. Ruby, J. Solid State Chem. 194 (2012) 328-335.

[44] N.A. Halasa, G. DePasquali, H.G. Drickamer, Phys. Rev. B 10 (1974), 154-164.

[45] E. Murad, U. Schwertmann, Am. Mineral. 65 (1980) 1044-1049.

[46] X. Wang, M. Zhu, L. K. Koopal, W. Li, W. Xu, F. Liu, J. Zhang, Q. Liu, X. Feng, D.L. Sparks, Environ. Sci. Nano 3 (2016) 190-202.

[47] F. Baron, S. Petit, M. Pentrák, A. Decarreau, J.W. Stucki, Am. Mineral. 102 (2017) 1501-1515.

[48] S. Suzuki, T. Suzuki, M. Kimura, Y. Takagi, K. Shinoda, K. Tohji, Y. Waseda, Appl. Surf. Sci. 169-170 (2001) 109-112.

[49] C.M. van Genuchten, J. Peña, S.E. Amrose, A.J. Gadgil, Geochim. Cosmochim. Acta 127 (2014) 285-304.

[50] S. Peulon, L. Legrand, H. Antony, A. Chaussé, Electrochem. Commun. 5 (2003) 208-213.

[51] A. Zegeye, G. Ona-Nguema, C. Carteret, L. Huguet, M. Abdelmoula, F. Jorand, Geomicrobiol. J. 22 (2005) 389-399.

[52] D. Li, M. Koike, L. Wang, Y. Nakagawa, Y. Xu, K. Tomishige, ChemSusChem 7 (2014) 510-522.

[53] G. Bancroft, A. Maddock, R. Burns, Geochim. Cosmochim. Acta 31 (1967) 2219–2246.

[54] G.B. Raupp, W.N. Delgass, J. Catal. 58 (1979) 337-347.

[55] G.B. Raupp, W.N. Delgass, J. Catal. 58 (1979) 348-360.

[56] E.E. Unmuth, L.H. Schwartz, J.B. Butt, J. Catal. 61 (1980) 242-255.

[57] F. Bødker, I. Chorkendorff, S. Mørup, Z. Phys. D 40 (1997) 152–154.

[58] C. E. Johnson, M.S. Ridout, T.E. Cranshaw, Proc. Phys. Soc. 81 (1963) 1079–1090.

[59] K. Nagorny, S. Bubert, J. Catal. 108 (1987) 112-134.

[60] M. Matsuyama, K. Ashida, O. Takayasu, T. Takeuchi, J. Catal. 102 (1986) 309-315.

[61] T. Mizushima, K. Tohji, Y. Udagawa, M. Harada, M. Ishikawa, A. Ueno, J. Catal. 112 (1988) 282-289.

[62] A.B. Merlo, V. Vetere, J.F. Ruggera, M.L. Casella, Catal. Commun. 10 (2009) 1665-1669.

[63] M. Koehle, R.F. Lobo, Catal. Sci. Technol. 6 (2016) 3018-3026.

[64] E. Marceau, A. Löfberg, J.M. Giraudon, F. Négrier, M. Che, L. Leclercq, Appl. Catal. A 362 (2009) 34-39.

[65] Z. Fu, Z. Wang, W. Lin, W. Song, S. Li, Appl. Catal. A 547 (2017) 248-255.

[66] Z. Li, Y.H. Huang, M. Zhu, X. Chen, H. Mei, J. Fuel Chem. Technol. 46 (2018) 54-58.

Fig. 1. ^{57}Fe Mössbauer spectra recorded on $Fe_{50}Ni_{50}/SiO_2$: a) after drying (RT); b) after reduction at 500°C under H_2 (RT); c) after reduction at 700°C under H_2 (RT); d) after reduction at 700°C under H_2 (-268°C). Blue, red: Fe^{3+} (a) or Fe^{2+} (b) contributions. Orange, brown: Fe(0) in Fe-Ni particles. Green: disordered Fe(0), in outer shells of Fe-Ni particles.

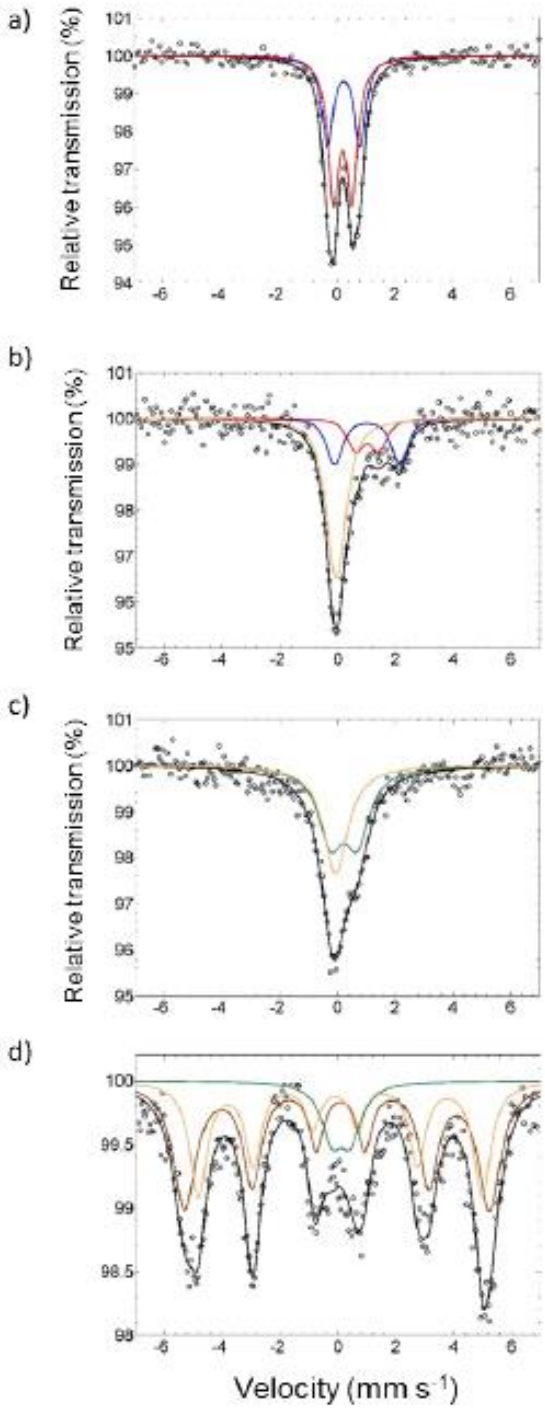

Fig. 2. EXAFS k^3-weighted oscillations and results of $k^3\chi(k)$ EXAFS fitting in R-space: of dried $Fe_{50}Ni_{50}/SiO_2$, a) at the Fe K edge, b) at the Ni K edge; and of $Fe_{50}Ni_{50}/SiO_2$ after reduction at 500°C: c) at the Ni K edge (spectrum recorded at RT under H_2). Black: experimental; red or green: fit. Interatomic distances R are listed in Table 2.

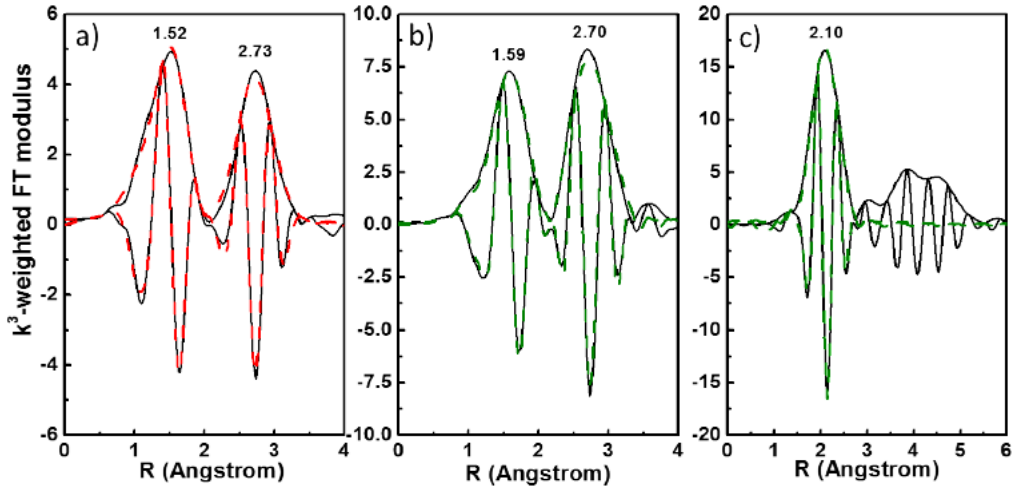

Fig. 3. Evolution as a function of DPU duration: a) of the infrared bands of $Fe_{50}Ni_{50}/SiO_2$ samples in the 500-1300 cm^{-1} region (ATR mode); b) of the Fe/Si and Ni/Si atomic ratios measured by ICP.

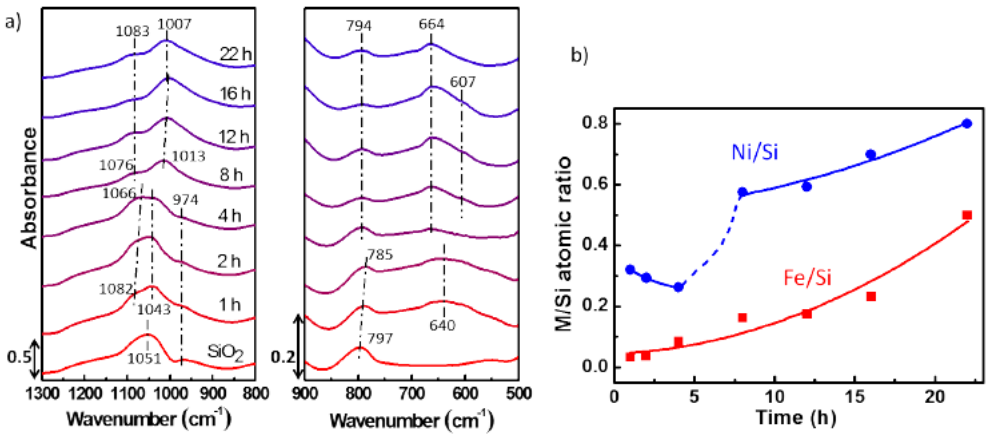

Fig. 4. X-ray absorption spectra recorded during the reduction of $Fe_{50}Ni_{50}/SiO_2$, simultaneously: a) at the Ni K edge; b) at the Fe K edge. c) MCR-ALS analysis of Ni reduction. d) Simultaneous evolution of the energy at the inflection point of the XANES spectra recorded at the Fe K edge.

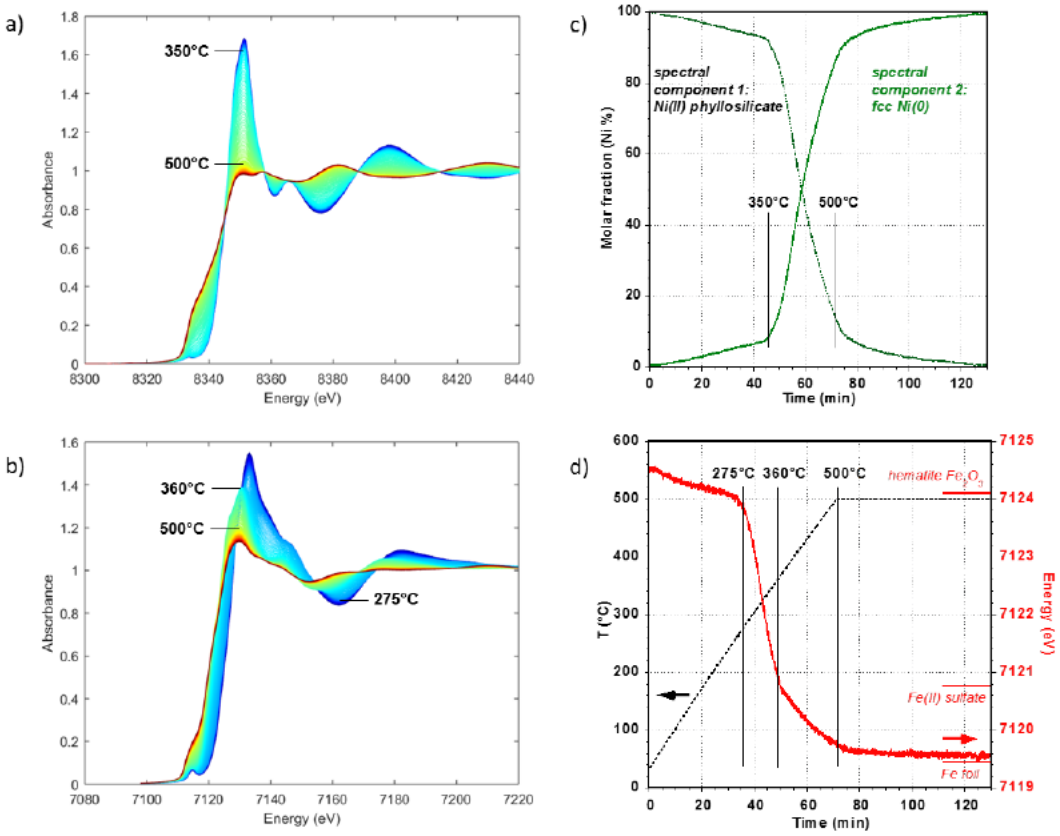

Fig. 5. X-ray diffractograms recorded as a function of temperature during the reduction of $Fe_{50}Ni_{50}/SiO_2$.

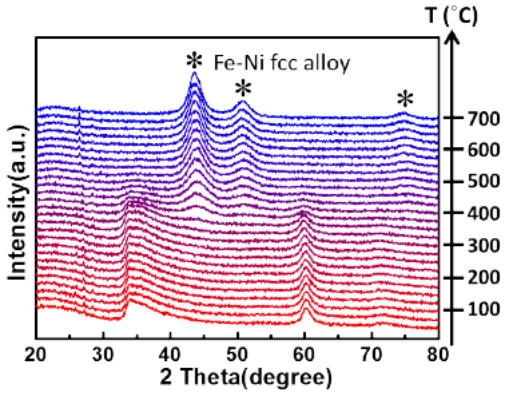

Fig. 6. Left: Bright field TEM micrographs of $Fe_{50}Ni_{50}/SiO_2$: a) after reduction at 500°C and exposure to air; b) after reduction at 700°C and exposure to air. Right: c) EDX mapping of $Fe_{50}Ni_{50}/SiO_2$ after reduction at 500°C and exposure to air (Fe: red; Ni: green).

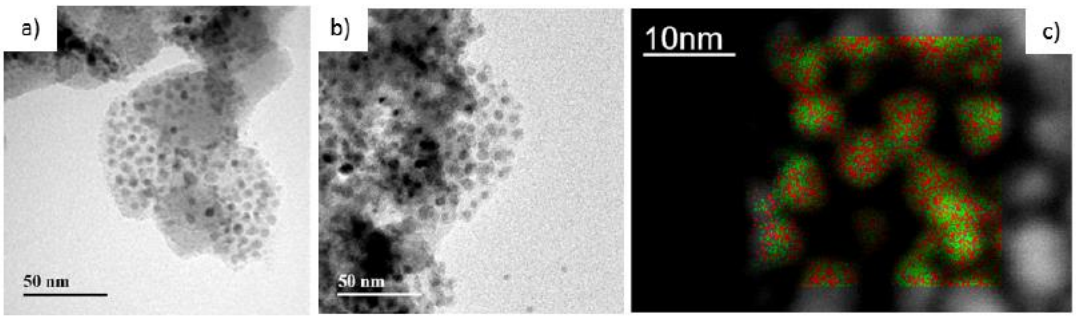

Scheme 1. Reaction pathways in the hydrogenation of furfural: blue routes, hydrogenation; red routes: hydrogenolysis of the C-O bond; green routes: etherification.

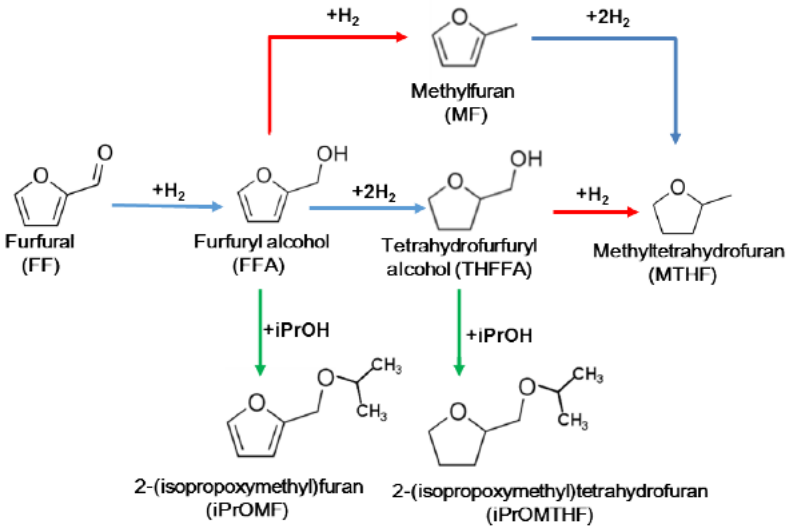

Table 1

^{57}Fe Mössbauer hyperfine parameters of sample $Fe_{50}Ni_{50}/SiO_2$ after drying and reduction. Spectra were recorded at room temperature (RT, 25°C) or low temperature (LT, -268°C).

Sample	Site	δ (mm.s^{-1})	Δ (mm.s^{-1})	Γ (mm.s^{-1})	Area (%)	B_{HF} (T)
$Fe_{50}Ni_{50}/SiO_2$	Fe(III) Oh	0.33(1)	0.65(2)	0.44(2)	64(4)	-
DPU, dried (RT)	Fe(III) Oh	0.36(1)	1.15(3)	0.45(4)	22(5)	-
$Fe_{50}Ni_{50}/SiO_2$	Fe(II) Oh	1.11(4)	2.25(8)	0.48(4)	26(3)	-
reduced at 500°C (RT)	Fe(II) Oh	1.12(6)	0.79(8)	0.48(4)	17(3)	-
	Fe(0) in Fe-Ni alloy	0.06(4)	0.00	0.64(9)	57(3)	-
$Fe_{50}Ni_{50}/SiO_2$	Fe(0) in Fe-Ni alloy	0.04(4)	0.00	1.03(4)	43(5)	-
reduced at 700°C (RT)	Fe(0)	0.35(6)	0.88(8)	1.03(4)	57(3)	-
$Fe_{50}Ni_{50}/SiO_2$	Fe(0) in Fe-Ni alloy	0.12(2)	0.00	0.90(1)	62(8)	32.5(4)
reduced at 700°C (LT)	Fe(0) in Fe-Ni alloy	0.16(2)	0.00	0.60(1)	28(1)	30.1(3)
	Fe(0), non magnetic	0.21(2)	0.67(7)	0.77(8)	10(1)	-

δ: isomer shift; Δ: electric quadrupole splitting; Γ: line width at half maximum; B_{HF}: magnetic hyperfine field

Table 2
Structural parameters determined from the EXAFS analysis of the spectra recorded at RT for the $Fe_{50}Ni_{50}/SiO_2$ catalyst after drying and after reduction at 500°C.

Sample	Absorbing atom	N, scattering atom	R (Å)	$\sigma^2.10^{-3}$ (Å^2)	R_F (%)	χ^2_υ
$Fe_{50}Ni_{50}/SiO_2$ DPU, dried	Ni	6 O * 6 Ni *	2.05 (1) 3.11 (1)	5 (1) 6 (1)	2.3	1688
$Fe_{50}Ni_{50}/SiO_2$ DPU, dried	Fe	6 O * 6 Ni *	1.99 (1) 3.11 (1)	11 (1) 13 (1)	0.5	697
$Fe_{50}Ni_{50}/SiO_2$ reduced at 500°C	Ni	11 (1) Ni	2.49 (1)	8 (1)	1.1	1067

N: Coordination number, *: fixed number; R: Distance between absorbing atom and neighbours; σ: Debye-Waller factor; R_F: reliability factor, which measures the relative misfit with respect to the data; χ^2_υ: reduced chi-square, which takes into account the uncertainty level in the data, as well as the number of free parameters allowed to vary in the fit. Simulations were done over Δk range = 3.5-10.5 Å^{-1}, ΔR = 1-3.4 Å for catalyst before reduction and 1-2.7 Å for catalyst after reduction, S_0^2 = 0.75, $E_0 + \Delta E_0$ = 7724 ± 2 eV at the Fe K edge, and 8340 ± 3 eV at the Ni K edge.

Table 3
Catalytic properties in the hydrogenation of furfural (FF) of the $Fe_{50}Ni_{50}/SiO_2$ and Ni_{100}/SiO_2 catalysts pre-reduced at 700°C.

	Conversion (%)	Yields (mmol)						Carbon balance (%)
		FFA	iPrOMF	THFFA	iPrOMTHF	MF	MTHF	
FF: 0.20 mmol								
$Fe_{50}Ni_{50}/SiO_2$	100	0.14	0.02	0.02	0	0.02	0	100
Ni_{100}/SiO_2	100	0	0	0.14	0.01	0	0.02	90
FF: 0.56 mmol								
$Fe_{50}Ni_{50}/SiO_2$	97	0.44	0.04	0.02	0	0.04	0	100
$Fe_{50}Ni_{50}/SiO_2$ [a]	*100*	*0.22*	*0.24*	*0.02*	*0*	*0.04*	*0.01*	*95*
Ni_{100}/SiO_2	100	0.01	0.07	0.12	0.10	0	0.22	93
FF: 1.00 mmol								
$Fe_{50}Ni_{50}/SiO_2$	100	0.74	0.15	0.04	0	0.04	0	97
Ni_{100}/SiO_2	99	0.02	0.11	0.08	0.07	0.20	0.37	85

Experimental conditions: catalyst mass: 10 mg; reduction conditions before reaction: 400°C under pure H_2; reaction temperature: 150°C; H_2 pressure: 20 bar; solvent: isopropanol; duration: 2 h. FFA: furfuryl alcohol; iPrOMF: 2-(isopropoxymethyl)furan; THFFA: tetrahydrofurfuryl alcohol; iPrOMTHF: 2-(isopropoxymethyl)tetrahydrofuran; MF: 2-methylfuran; MTHF: 2-methyltetrahydrofuran

[a] without pre-reduction at 700°C

Supplementary material

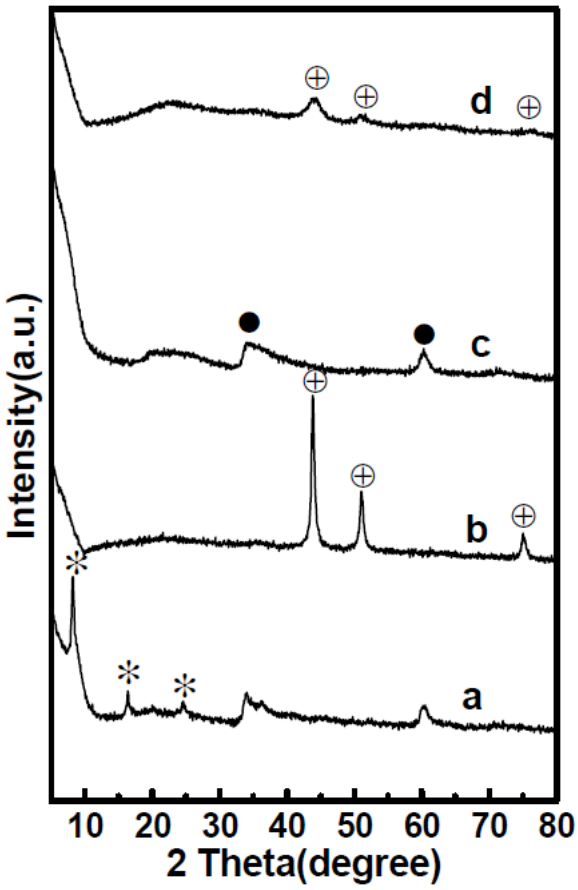

Fig. S1. X-ray diffractograms of $Fe_{50}Ni_{50}/SiO_2$ prepared without Ar degassing: a) recorded after drying, b) recorded after reduction at 700°C; and prepared with Ar degassing: c) recorded after drying, d) recorded after reduction at 700°C.

* hydrohonessite $[Ni^{2+}_{8-x}\ Fe^{3+}_{x}\ (OH)_{16}][SO_4^{2-}\ .\ 7\ H_2O\ .\ NiSO_4]$ (E. H. Nickel, J. E. Wildman, Mineral. Mag. 44 (1981) 333-337; L. H. Garófalo Chaves, J. E. Curry, D. A. Stone, M. D. Carducci, J. Chorover, Rev. Bras. Ci. Solo 33 (2009) 1115-1123)

+ fcc Fe-Ni alloy

• 1:1 phyllosilicate

See main text for the identification of the latter two phases.

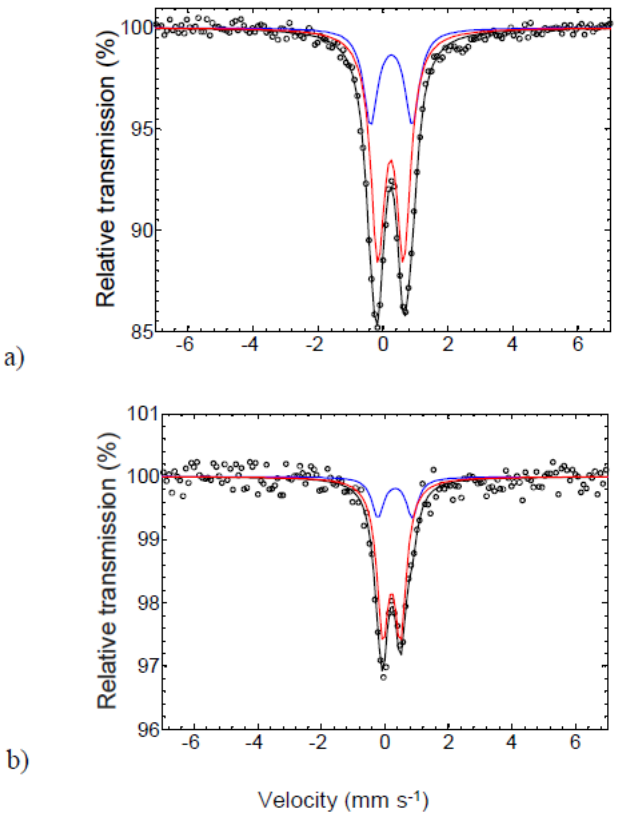

Fig. S2. ^{57}Fe Mössbauer spectra recorded at room temperature on: a) dried $Fe_{75}Ni_{25}/SiO_2$; b) dried $Fe_{25}Ni_{75}/SiO_2$.

Table S1

^{57}Fe Mössbauer hyperfine parameters of dried samples $Fe_{75}Ni_{25}/SiO_2$ and $Fe_{25}Ni_5/SiO_2$. Spectra were recorded at room temperature (25°C).

Sample	Site	δ (mm.s^{-1})	Δ (mm.s^{-1})	Γ (mm.s^{-1})	Area (%)
$Fe_{75}Ni_{25}/SiO_2$	Fe(III) Oh	0.35(1)	0.78(2)	0.48(1)	67(3)
DPU, dried	Fe(III) Oh	0.37(1)	1.25(3)	0.48(1)	33(3)
$Fe_{25}Ni_{75}/SiO_2$	Fe(III) Oh	0.33(4)	0.55(3)	0.45(4)	78(5)
DPU, dried	Fe(III) Oh	0.43(4)	1.08(8)	0.45(4)	22(5)

δ: isomer shift; Δ: electric quadrupole splitting; Γ: line width at half maximum; B_{HF}: magnetic hyperfine field

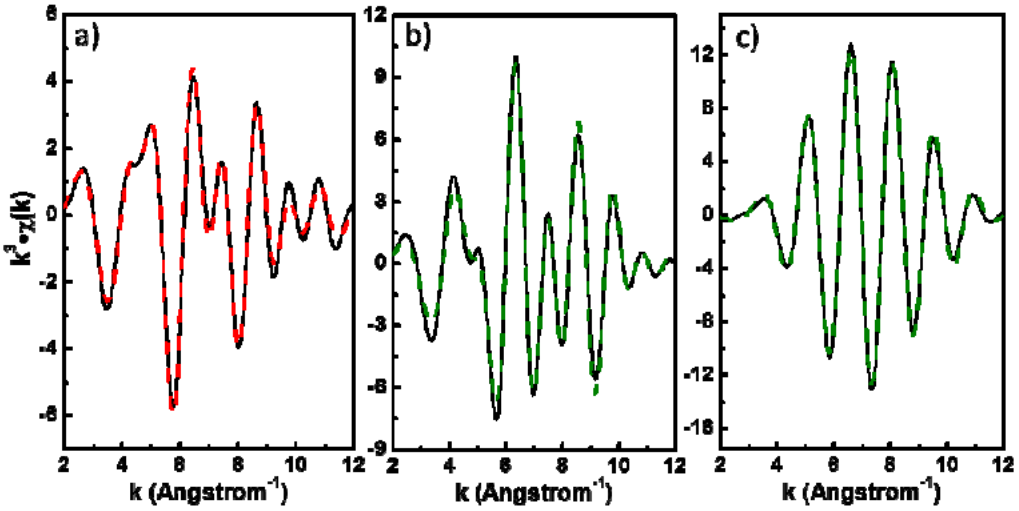

Fig. S3. EXAFS k^3-weighted oscillations and results of k^3 χ(k) EXAFS fitting in k-space: of dried $Fe_{50}Ni_{50}/SiO_2$, a) at the Fe K edge, b) at the Ni K edge; and of $Fe_{50}Ni_{50}/SiO_2$ after reduction at 500°C: c) at the Ni K edge, first shell (spectrum recorded at RT under H_2). Black: experimental; red or green: fit.

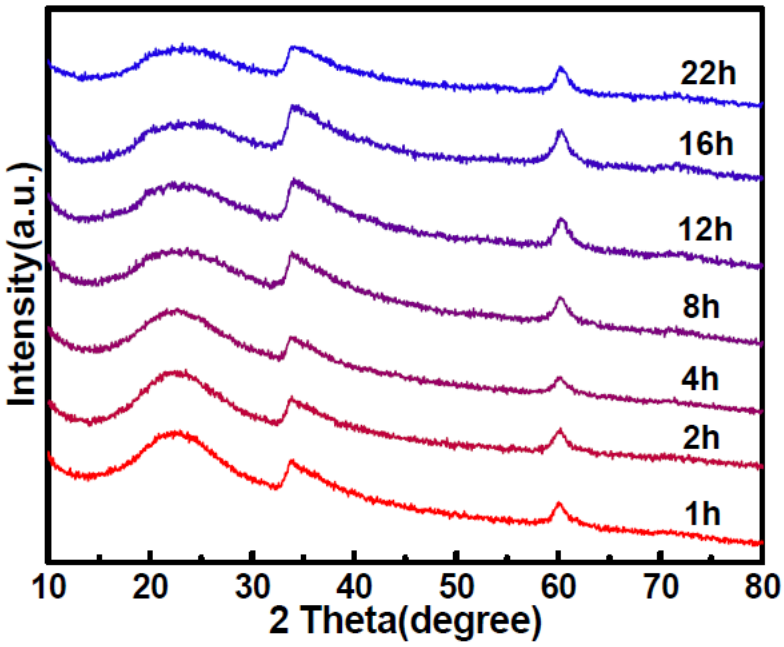

Fig. S4. X-ray diffractograms recorded in ambient conditions on $Fe_{50}Ni_{50}/SiO_2$ samples prepared with different durations of DPU.

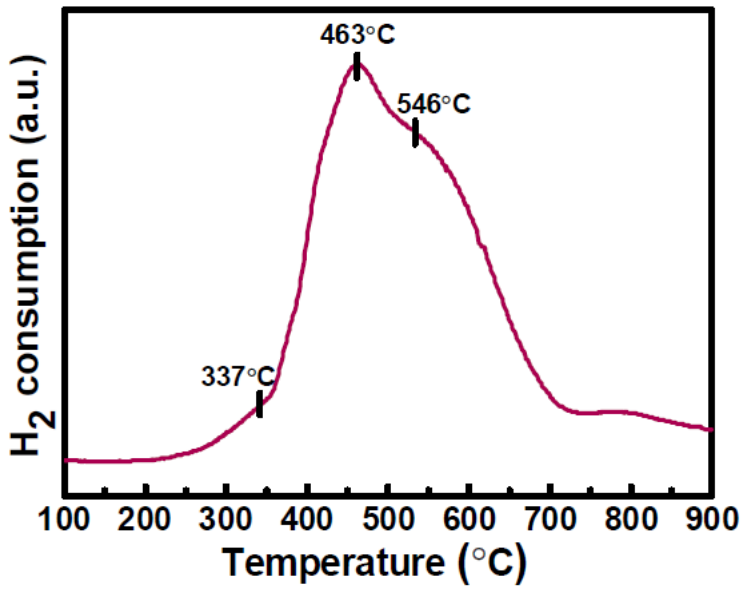

Fig. S4. Temperature-reduction profile of $Fe_{50}Ni_{50}/SiO_2$ after storage in air and drying at 60°C (H_2(5%)/Ar, flow rate: 50 mL min^{-1}, heating ramp: 7.5°C min^{-1}).

Multivariate Curve Resolution by Alternating Least Squares (MCR-ALS) analysis applied to the reduction of $Fe_{50}Ni_{50}/SiO_2$.

The Multivariate Curve Resolution by Alternative-Least Squares (MCR-ALS) methodology was used herein for the identification of the successive stages of reduction of $Fe_{50}Ni_{50}/SiO_2$ at the Ni and Fe K edges. In this methodology, XAS spectra are considered to originate from a linear combination of individual spectral components weighted by their abundance at any given temperature. Unlike the more classical linear combination procedure involving reference compounds, no hypothesis on the individual components is initially required in the MCR-ALS procedure. The series of normalized experimental spectra D is defined as a matrix resulting from the combination of three matrices: C (concentration of the pure components); S (normalized XAS spectral of pure components); and E (experimental uncertainties), following the matricial equation: $D = C\,S^T + E$ (where S^T is the transposed matrix of S). The principle of the MCR-ALS analysis is to identify a likely set of concentrations C (varying along the series) and spectra S (constant along the series) which can explain the whole set of D, by iteration and least-squares minimization of the E matrix. The rank of the matrix (the number of components) is initially determined by Principal Component Analysis. The matrix of concentrations C contains only positive values and the matrix S contains only normalized spectral components with a positive absorbance.

XAS spectral components S are thus extracted by a purely mathematical method, without any initial hypothesis on the nature of the associated compounds. MCR-ALS components can only be validated after checking their chemical meaningfulness by comparison with spectra of compounds already identified in the mixture (as is the case here for nickel), or with plausible models in accordance with the chemistry of the system. The recognized limits of the MCR-ALS method with respect to XAS analysis lie in:

(i) the fact that *two spectral components* can correspond to the initial and final states of *the same chemical species* undergoing progressive ordering or disordering with changes of temperature;

(ii) on the opposite, the possible *concomitant evolution of two distinct chemical species* that appear as *merged in a single spectral component*.

The EXAFS analysis of components existing at higher temperatures is also challenged by the damping of the oscillations due to an increased Debye-Waller factor.

For this reason, the meaningfulness of the spectral components identified during reduction at the Fe K edge is interpreted here not as spectra characteristic of single species, but in accordance with the evolution of the position in energy of the Fe edge, with the simultaneous evolutions observed at the Ni K edge, and through the similarity or shifts of the oscillations and peaks on the Fourier transforms. MCR-ALS analysis at the Fe K edge will not be discussed on a quantitative basis.

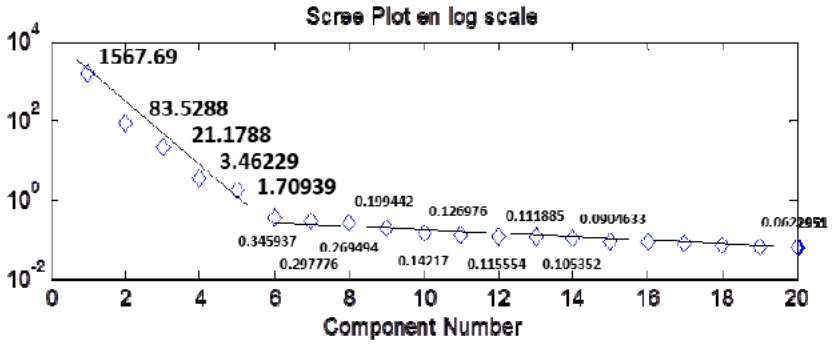

Principal Component Analysis by Singular Value Decomposition (PCA-SVD) was used to estimate the number of chemically relevant components involved in the reduction process at the Fe K edge. A plot of the eigenvalues sorted as a function of components, also named Scree plot, has been used for such an estimation. As the components are sorted in order of decreasing contribution to the total variance, the separation between the linearly aligned eigenvalues of the first Principal Components, which are the most important ones, and those belonging to the asymptotic trend are used for the determination of the number of components to consider for the MCR-ALS analysis. The Scree plot above displays a break of slope after the 5th component, indicating than the important components to retain for explaining most of the variance of the system are the first 5 components.

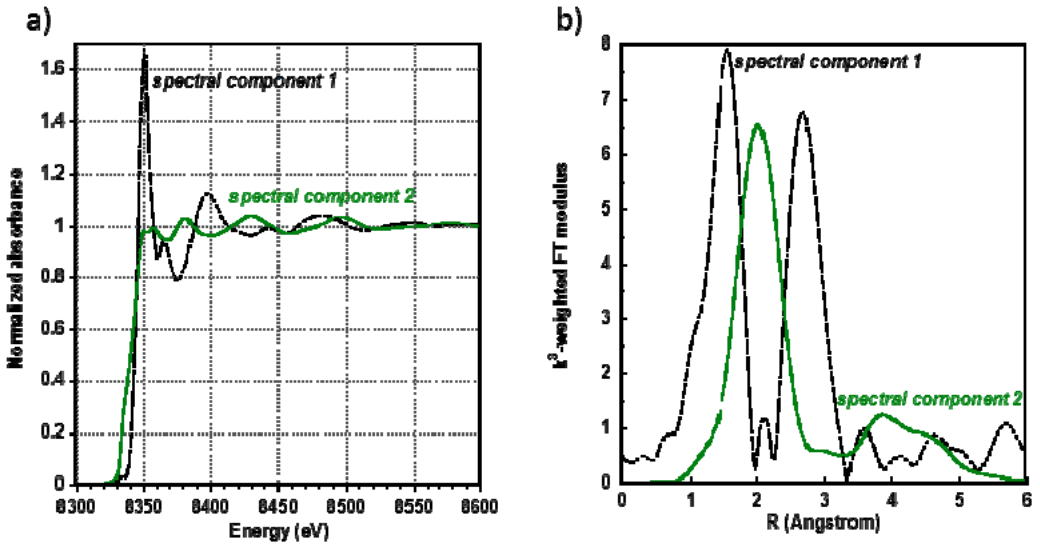

Fig. S6. MCR-ALS spectral contributions to the spectra recorded at the Ni K edge during the reduction of $Fe_{50}Ni_{50}/SiO_2$: a) XANES region; b) Fourier transforms.

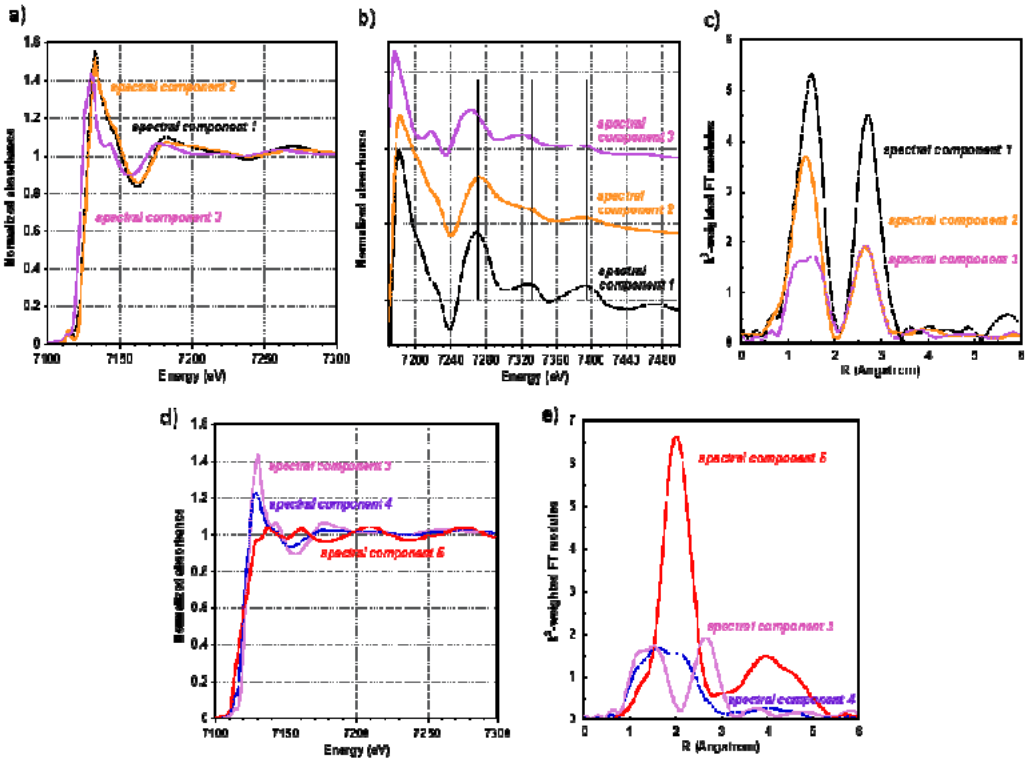

Fig. S7. MCR-ALS spectral contributions to the spectra recorded at the Fe K edge during the reduction of $Fe_{50}Ni_{50}/SiO_2$: a) XANES region, b) oscillations (curves shifted upwards) and c) Fourier transforms of spectral components 1, 2 and 3; d) XANES region and e) Fourier transforms of spectral components 3, 4 and 5.

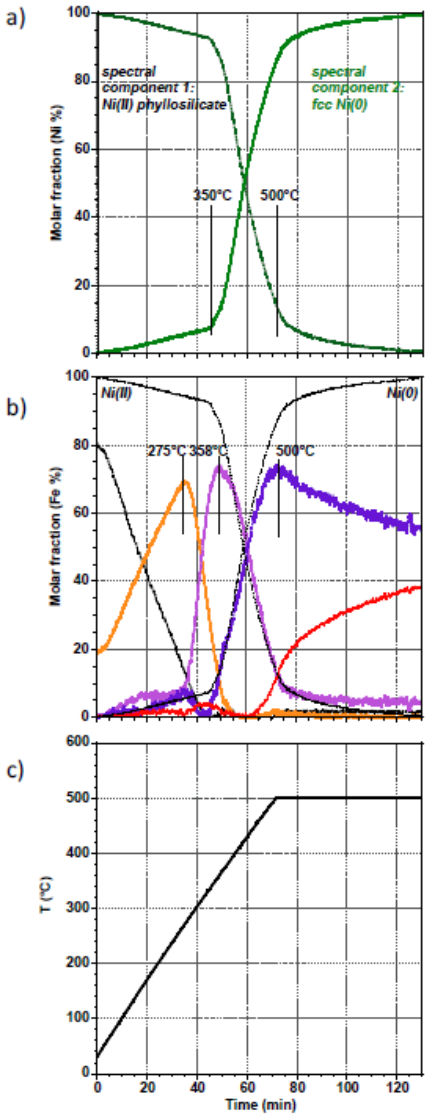

Fig. S8. MCR-ALS analysis of the reduction of $Fe_{50}Ni_{50}/SiO_2$: a) at the Ni K edge (cf. Fig. 4c and S4); b) at the Fe K edge (cf. Fig. S5); c) temperature curve as a function of time.

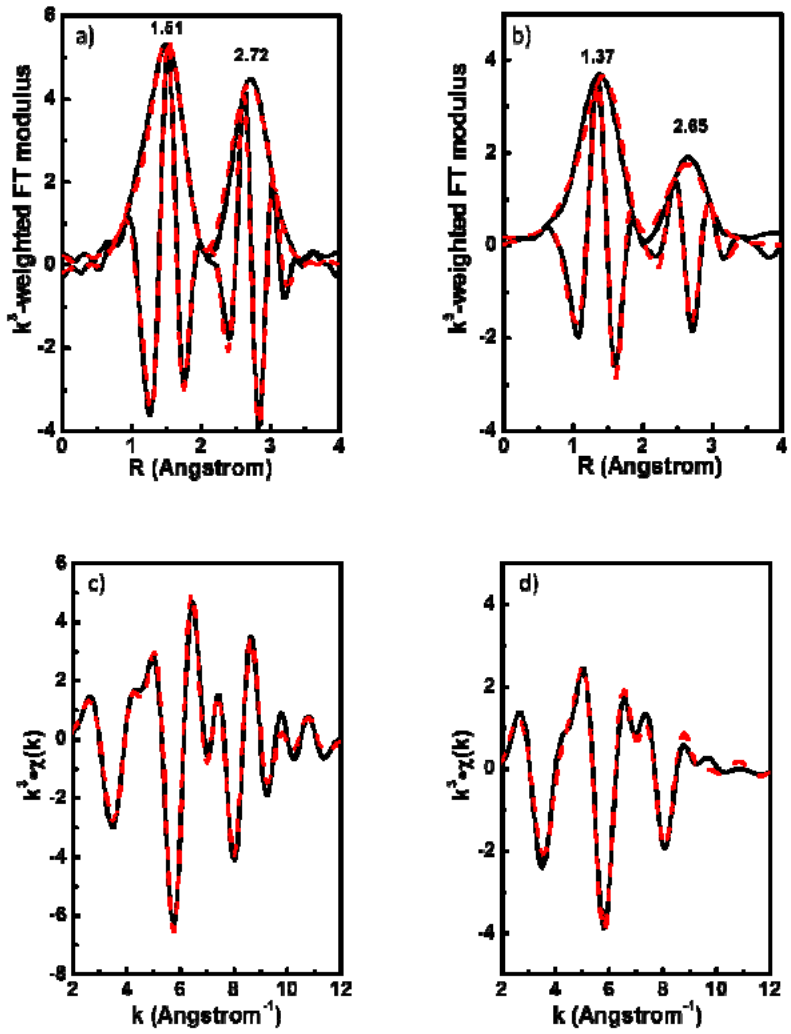

Fig. S9. EXAFS k^3-weighted oscillations and results of k^3 χ(k) EXAFS fitting in R-space of: a) the first component (black, Fig. S7 and S8), b) the second component (orange, Fig. S7 and S8). EXAFS k^3-weighted oscillations and results of k^3 χ(k) EXAFS fitting in k-space of: c) the first component (black, Fig. S7 and S8), d) the second component (orange, Fig. S7 and S8) Black: experimental; red: fit. Interatomic distances R are listed in Table S2.

Table S2

Structural parameters determined from the EXAFS analysis of the two spectral components presented in Fig. S9.

	Absorbing atom	N, scattering atom	R (Å)	$\sigma^2.10^{-3}$ (Å^2)	R_F (%)	χ^2_υ
$Fe_{50}Ni_{50}/SiO_2$ DPU, dried (Table 2)	Fe	6 O * 6 Ni *	1.99 (1) 3.11 (1)	11 (1) 13 (1)	0.5	697
1st compoment (black curves, Fig. S7 and S8)	Fe	6 O * 6 Ni *	1.99 (1) 3.12 (1)	9 (1) 11(1)	1.0	1291
2nd compoment (orange curves, Fig. S7 and S8)	Fe	6 O * 6 Ni *	1.95 (1) 3.10 (1)	14 (1) 22 (1)	1.5	1824

N: Coordination number, *: fixed number; R: Distance between absorbing atom and neighbours; σ: Debye-Waller factor; R_F: reliability factor, which measures the relative misfit with respect to the data; χ^2_υ: reduced chi-square, which takes into account the uncertainty level in the data, as well as the number of free parameters allowed to vary in the fit. Simulations were done over Δk range = 3.5-10.5 Å^{-1}, ΔR = 1-3.4 Å for catalyst before reduction and 1-2.7 Å for catalyst after reduction, S_0^2 = 0.75, $E_0 + \Delta E_0 = 7724 \pm 2$ eV at the Fe K edge.

Phase	JCPDS file	a (nm)
$Fe_{64}Ni_{36}$	PDF 00-047-1405	0.35922
$Fe_{45}Ni_{55}$	PDF 04-003-2425	0.35758
$Fe_{40}Ni_{60}$	PDF 04-004-8867	0.35632
$Fe_{27}Ni_{73}$	PDF 04-004-8203	0.35480
$Fe_{25}Ni_{75}$	PDF 04-004-6754	0.35525
$Fe_{18}Ni_{82}$	PDF 04-003-2245	0.35440
Ni_{100}	PDF 04-010-6148	0.35285

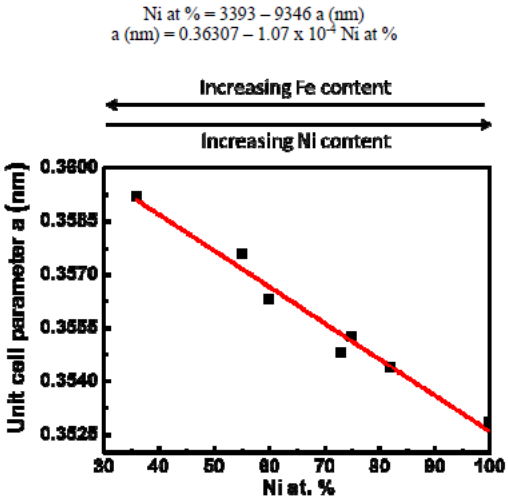

Fig. S10. Correlation between the unit cell parameter *a* of Fe-Ni alloys and the nickel atomic content (based on the values of *a* listed in the table above).

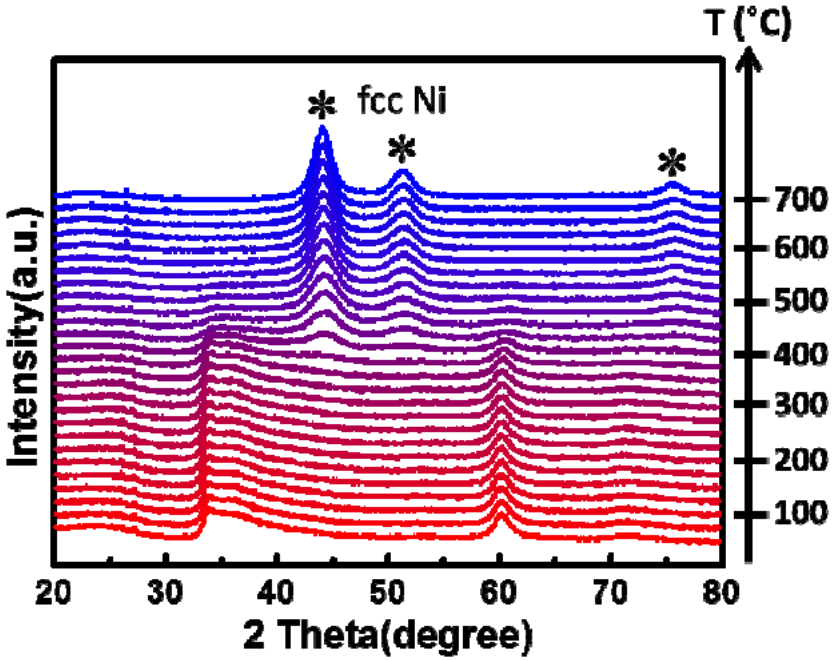

Fig. S11. X-ray diffractograms recorded as a function of temperature during the reduction of Ni_{100}/SiO_2 under H_2 (3%)/N_2.

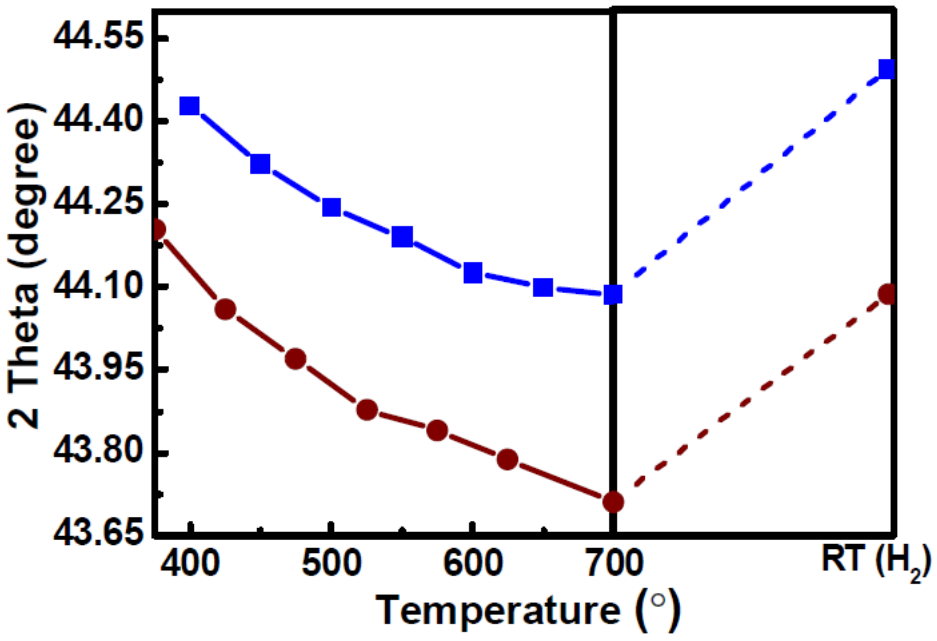

Fig. S12. Evolution of the position of the (111) Bragg reflection for Fe-Ni (brown) and Ni (blue) nanoparticles on $Fe_{50}Ni_{50}/SiO_2$ and Ni_{100}/SiO_2 during heating under H_2 and after cooling to room temperature under H_2 (RT).

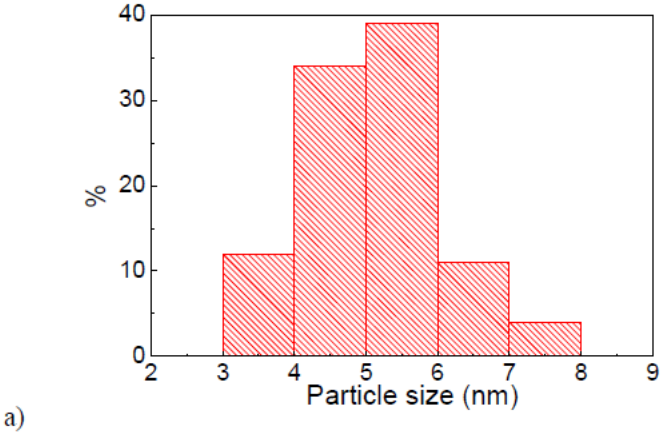

a)

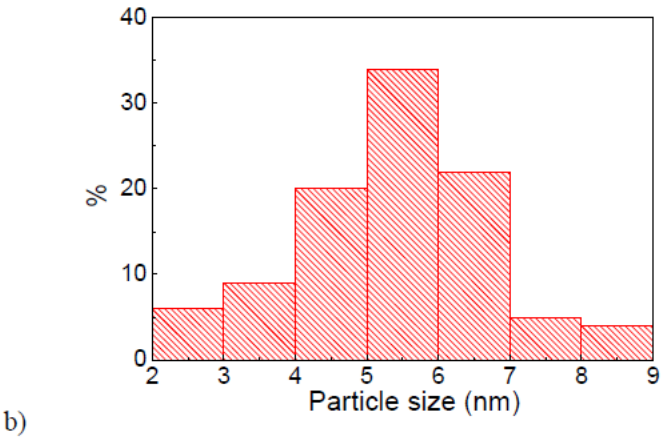

b)

Fig. S13. Particle size distributions measured by TEM for $Fe_{50}Ni_{50}/SiO_2$: a) after reduction at 500°C and exposure to air; b) after reduction at 700°C and exposure to air.

Table S3

EDX point scan measurements on 28 individual particles from $Fe_{50}Ni_{50}/SiO_2$ reduced at 500°C and exposed to air.

	Fe at %	Ni at %
	30.58	69.42
	28.78	71.22
	46.81	53.19
	27.96	72.04
	40.81	59.19
	36.27	63.73
	24.19	75.81
	38.94	61.06
	37.09	62.91
	40.92	59.08
	16.28	83.72
	14.37	85.63
	24.91	75.09
	38.32	61.66
	28.32	71.68
	30.24	69.76
	39.07	60.93
	30.42	69.58
	30.92	69.08
	18.82	81.18
	28.57	71.43
	35.70	64.30
	24.55	75.45
	31.78	68.22
	45.94	54.06
	18.81	81.19
	25.28	74.72
	33.21	66.79
Average:	31.00%	69.00%

a)

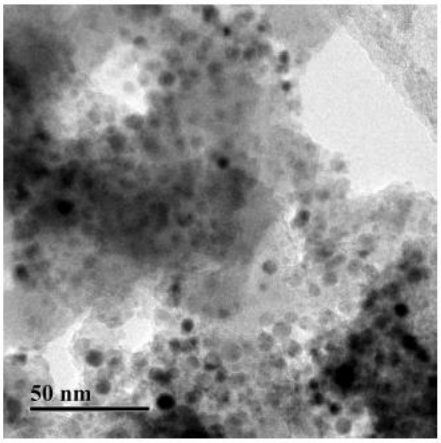

b)

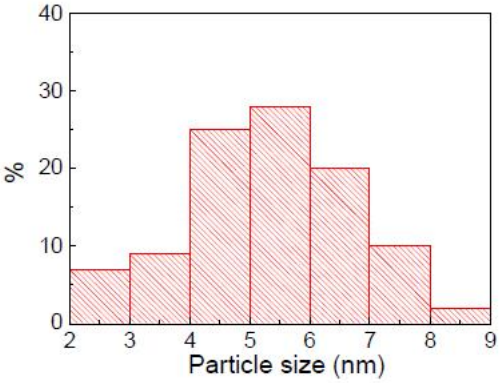

Fig. S14. a) Bright field TEM micrograph of Ni_{100}/SiO_2 after reduction at 700°C and exposure to air. b) Particle size distribution measured by TEM for Ni_{100}/SiO_2 after reduction at 700°C and exposure to air.